Tunnelling and Underground Space Technology 147 (2024) 105720

Contents lists available at ScienceDirect

Tunnelling and Underground Space Technology incorporating Trenchless Technology Research

journal homepage: www.elsevier.com/locate/tust

Enhancing blast mitigation in tunnels with expansion chamber subjected to high explosives detonations for protecting underground facilities

Jinwon Shin [a], Seungki Pang [b], Woosuk Kim [c,*]

[a] Department of Architectural Engineering, Catholic Kwandong University, Gangneung-si 25601, South Korea
[b] Department of Architecture, Kyungmin University, Uijeongbu 11618, South Korea
[c] Department of Architectural Engineering, Kumoh National Institute of Technology, Gumi-si 39177, South Korea

A R T I C L E I N F O

Keywords:
Protective tunnel
Overpressure reduction
Detonation
Expansion chamber
Computational fluid dynamics analysis

A B S T R A C T

This paper presents a numerical investigation into the effect of expansion chamber in mitigating overpressures and impulses in protective tunnels subjected to detonation of high explosives. Blast shockwave propagation in a protective tunnel, with dimensions of 160 m in length, 8.9 m in width and 7.2 m in height, was simulated using a computational fluid dynamics code, Viper::Blast. The design parameters of the expansion chamber cover a broad spectrum chamber lengths between 6.1 and 12.1 m, widths spanning from 10.7 to 97 m, length-to-width ratios from 0.0 (indicating no chamber) to 5.0, heights of 8.0 and 14.9 m, and chamber-to-tunnel width ratios in the range of 1.2 to 10.9 m. Two charge weights of 1000 and 2000 kg of TNT were employed to assess their influences. To ensure the reliability of the CFD model, mesh sensitivity analysis, overpressure stability assessments, and validation studies were undertaken. A parametric analysis was then conducted using the validated model to derive an optimal design for the expansion chamber within the specified tunnel. Recommendations for incorporating an expansion chamber into protective tunnels under blast events are provided.

1. Introduction

Blast-resistant design aims to safeguard personnel, equipment, and materials from both internal and external detonations. This design approach finds widespread application in military facilities, nuclear power plants, critical national infrastructure, and social infrastructure. In smaller protective facilities, only blast-resistant doors are commonly utilized. However, in larger-scale facilities such as tunnels, the installation of blast valves becomes essential. These valves serve to protect personnel and facilities from blast overpressures and to ensure proper ventilation for equipment operation (Pang et al., 2018; Pang and Shin, 2021; Sharma et al., 2016; Shin et al., 2023). The rating and cost of blast valves are determined based on the magnitude of blast overpressures. Depending on the scale of the facility, rating required, and blast overpressure levels, the number of blast valves needed can reach several hundred, significantly impacting the construction costs.

In underground protective facilities, access is commonly provided through tunnels. If a detonation occurs either outside or inside the tunnel, shockwaves are generated and propagate through the tunnel. In general, blast overpressures in open spaces tend to rapidly decrease with distance or an increase in volume (Dusenberry, 2010). However, inside the tunnel, blast energy becomes confined within the interior, leading to repeated shockwave reflections by the tunnel walls and amplification of the overpressures, that is, the internal overpressures gradually decrease with distance due to the confinement of the blast shockwaves within the tunnel (Liu et al., 2008; Machniewski and Molga, 2022). As a result, significant levels of blast overpressure can occur in underground protective facilities located at considerable distances from the detonation point (Hetherington and Smith, 1994; Kinney and Graham, 1962; Kinney et al., 1986; Shin and Pang, 2022). Considering this, it becomes essential to implement measures that account for the environmental characteristics of the tunnel to effectively reduce the blast overpressures and impulses within the tunnel and optimize the construction costs.

To address this challenge, Hager et al. (1996) proposed a method involving the installation of chambers into the sidewalls of a tunnel. These side chambers served as storage areas and facilitated the partial propagation of blast shockwaves into them, resulting in a decrease in the overpressures at the shock front. While the overpressure reduction effect of this chamber installation was reasonably analyzed, applying these findings to real protective tunnels poses practical difficulties. The limited consideration of design parameters for tunnels and chambers, coupled with variations in specifications and shapes among real tunnels,

* Corresponding author.
E-mail address: kimw@kumoh.ac.kr (W. Kim).

https://doi.org/10.1016/j.tust.2024.105720
Received 4 October 2023; Received in revised form 9 January 2024; Accepted 17 March 2024
Available online 26 March 2024

makes direct application challenging.

The study conducted by Zhao et al. (2015) presented a method of applying an expanded cross-section to a specific part of a tunnel with a constant profile. This approach momentarily increases the volume and reduces the blast overpressures within the subsequent section of the tunnel. Although this method proves to be a simple and effective way of mitigating blast overpressures in protective tunnels, the limitations of the study lie in its specificity to certain detonation conditions and design parameters, and the quantitative effects remain unclear. Additionally, the practical application of these findings to various tunnel specifications presents challenges. In recent years, other various methods for mitigation techniques of blast overpressures were reported by Isaac et al. (2022). They summarized geometric designs for shock attenuation using perforated barriers, baffle plates, vertical barriers, smooth double-wall duct tube, and so on. These methods can be selectively considered for tunnel design, but quantitative evaluation of the overpressure reduction of each method according to design variables is insufficient to adopt the corresponding methods. In the meantime, Shin and Pang (2022) introduced a method aimed at reducing blast overpressure in protective tunnels by considering the shape of the tunnel entrance and the depth of the blast pocket exposed to external detonations. However, it is essential to note that this method only applies to the entrance section of the tunnel, leaving other sections without a viable solution. Accordingly, further studies that encompass diverse detonation conditions, tunnel design, and environmental factors are imperative to effectively attenuate blast overpressures in protective tunnels.

This study presents a numerical analysis to investigate the reduction of blast shockwave overpressures using an expansion chamber in a specific protective tunnel with a defined cross-sectional profile. The protective tunnel subjected to detonation was modeled using a computational fluid dynamics (CFD) code, Viper::Blast (Stirling, 2021). To ensure the numerical accuracy, a mesh sensitivity study based on the h-refinement strategy (Cook, 2002; Shin, 2014) was carried out to determine the appropriate mesh size. Validation of the CFD model (ASME, 2006; Shin et al., 2015a) was achieved using the empirical design chart available in United Facilities Criteria (UFC) 3–340-02 (DoD, 2008), a U. S. Department of Defense (DoD) guideline for blast-resistant design, developed by Kingery and his co-workers (Kingery and Pannill, 1964; Kingery, 1966; Kingery and Bulmash, 1984; Shin et al., 2015b). The overpressure stability during shock wave propagation was also examined. A parametric analysis was then conducted using the validated model varying design parameters including the length-to-width ratio of expansion chamber, chamber height, chamber-to-tunnel width ratio, and charge weight. Based on the numerical analysis, design recommendations for the expansion chamber to reduce blast overpressures were provided.

2. Protective tunnels with expansion chamber

The protective tunnel considered was designed based on the specifications of that described in Shin and Pang (2022). The tunnel considered is a passageway for access to a government-integrated data center in Gongju city, of National Information Resources Service (2016) of Ministry of the Interior and Safety (MOI) in South Korea. Since the data center is classified as National Security Facilities of Korean government so that it is built underground for security and protection purposes. Blast valves are often installed to secure the necessary air volume for permanent personnel in underground data centers and military command facilities installed within protective tunnels, as well as air volume to remove heat from various equipment. For reduction of overpressures on blast valves for external air intake from detonation, this study was intended to present guidelines for tunnel design.

A full-scale model of the tunnel was employed for numerical simulations to accurately reflect real-world blast scenarios and avoid the potential inaccuracies or limitations often associated with scaled-down physical models. Its basic configuration has a straight shape with a length of 160 m, a width of 8.9 m, a height of 7.2 m, and a wall thickness of 1.2 m. A computational fluid dynamics (CFD) software, specialized in blast simulation, was employed to investigate the effect of overpressure and impulse reduction by an expansion chamber when the blast shockwave propagates through the tunnel. A specific section of the tunnel was defined as the expansion chamber, which has a relatively larger volume compared to the tunnel width. The design range of the expansion chamber was determined with reference to the work of Zhao et al. (2015).

When blast waves from detonation propagate through the tunnel and enter the expansion chamber, overpressures are distributed instantaneously in the relatively larger space, and this allows for a reduction in the overpressures. The design parameters for optimizing the expansion chamber include length (6.1 to 12.1 m), width (10.7 to 97 m), height (8 and 14.9 m), length-to-width ratio (0.0 (no chamber) to 5.0), and chamber-to-tunnel width ratio (1.2 to 10.9). Fig. 1(a) shows the baseline model of a protective tunnel without an expansion chamber, and Fig. 1 (b) shows a protective tunnel applying an expansion chamber, with a width approximately three times the tunnel width, and a length-to-width ratio of 1.0, and a height of 8.0 m.

3. Modeling of protective tunnels exposed to detonation

3.1. CFD modeling

In the realm of simulating blast wave propagation in tunnels, the precision and accuracy of numerical techniques are paramount. Computational Fluid Dynamics (CFD) codes, often referred to as hydrocodes, are instrumental in this domain. These codes excel at computing the dynamics of compressible fluids across regular Cartesian grids and are frequently integrated with finite element methods to assess structural impacts.

A recently developed CFD code, Viper::Blast (Stirling, 2021), crafted by Stirling Simulation Services Limited (SSSL) was selected for blast analysis. This choice was motivated by the need for an advanced tool capable of handling the complexities involved in large-scale models of protective tunnels. Viper::Blast distinguishes itself through its utilization of an analysis methodology rooted in the work of Rose (2010). This approach is complemented by the integration of the AUSMDV numerical algorithm (Wada and Liou, 1994), renowned for its precision in fluid dynamics simulations, and the MUSCL-Hancock temporal integration method (Toro, 2009), known for its computational efficiency.

A core innovation in Viper::Blast is its optimization for NVIDIA Graphics Processing Units (GPUs). This advancement targets reducing analysis time and cutting down on project expenses, a crucial consideration in large-scale simulations. The GPU-based hardware acceleration technique employed by Viper::Blast offers a significant advantage over the multiple CPU-based approaches used in alternative CFD codes such as LS-DYNA (LST, 2021) and Autodyn (ANSYS, 2018). This is particularly evident in scenarios requiring extensive computational resources. For instance, a comparative study conducted by Stirling (2020) on blast wall simulations using different CFD codes revealed the efficiency of Viper::Blast. In simulations involving seven million cells, OpenFOAM/BlastFOAM 3.0 (Heylmun et al., 2019) and ANSYS Autodyn recorded wall-clock times of 10.4 and 13.4 h, respectively. In stark contrast, Viper::Blast 1.14.0 completed the same task in only 0.12 h, marking a staggering reduction in analysis time by over 98 %. This remarkable efficiency demonstrates the effectiveness of Viper::Blast in modeling and simulating blast events in large-scale protective tunnels, making it a superior choice for our study.

To ensure numerical accuracy and minimize computational costs, the blast simulations were conducted in two stages. The early stage of detonation of combustion products was simulated in the one-dimensional (1D) domain with radial symmetry until the blast waves reached reflecting boundaries. The overpressure data obtained from the 1D analysis was then remapped to the three-dimensional (3D) domain in

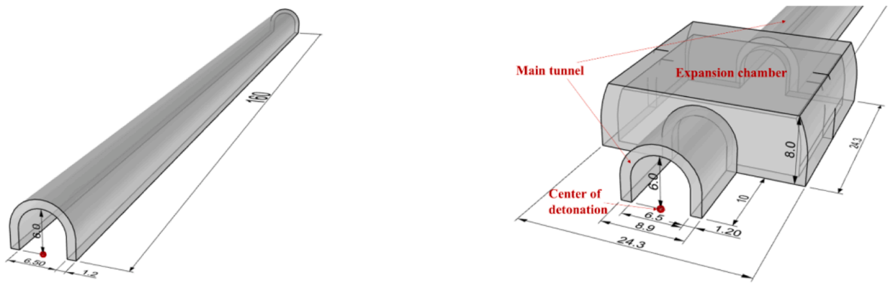

(a) Baseline model of protective tunnel (b) Tunnel with expansion chamber

Fig. 1. Protective tunnel and expansion chamber.

which the tunnel was modeled (ANSYS., 2005; Gabriel et al., 2023; Shin and Lee, 2016), allowing for the simulation of effects such as reflection and diffraction of blast waves (Krauthammer, 2008; Zhao et al., 2021). Given the nature of CFD analysis, very small mesh sizes were required to achieve the accuracy in the initial overpressure of the detonation (Sherkar, 2010; Shin et al., 2014). However, because the initial detonation expansion was simulated in 1D, a relatively larger mesh was permitted in the 3D analysis.

The 1D model consists of a high explosive of TNT and the surrounding air. The detonation of TNT was simulated using the Jones-Wilkins-Lee (JWL) equation of state (EOS) to calculate the overpressures caused by the expansion of the explosive materials (Fickett and Davis, 2000; Mohotti et al., 2023; Shin et al., 2014):

$$p = A\left(1-\frac{w}{R_1V}\right)e^{-R_1V} + B\left(1-\frac{w}{R_2V}\right)e^{-R_2V} + \frac{w}{V}E \tag{1}$$

where p is pressure, A, B, R_1 and R_2 are constants calibrated from test data, ω is adiabatic constant, V is relative volume, and E is specific energy. The values of the JWL EOS parameters were obtained from the LLNL Explosives Handbook (Dobratz and Crawford, 1981), as listed in Table 1. Afterburning was not modeled due to potential limitations resulting from the incomplete mixing of fuel with available oxygen and a temperature below the ignition threshold (1800 K) of constituent fuels of TNT (Castellano et al., 1982). The tunnel model was entirely filled with air, and the ideal gas EOS was used to model air with an initial ambient pressure of 101.3 kPa:

$$p = (\gamma-1)\frac{\rho}{\rho_0}e \tag{2}$$

Table 1
EOS parameters for modeling TNT and air.

TNT			Air		
Parameter		Value	Parameter		Value
Equation of state (EOS)		JWL	Equation of state (EOS)		Ideal gas
Density	ρ_{TNT}, kg/m^3	1540	Density	P_{air}, kg/m^3	1.225
Specific energy	E_0, kJ/kg	5400	Initial internal energy	e, kJ/kg	206.8
Calibrated constant	A_1, GPa	371.2	Specific heat ratio	γ	1.4
Calibrated constant	R_1	4.15	Ambient pressure	P_0, kPa	101.3
Calibrated constant	A_2, GPa	3.231	Initial temperature	T, K (°C)	288 (15)
Calibrated constant	R_2	0.95			
Adiabatic constant	ω	0.3			
CJ detonation velocity	D_{cj}, m/s	6930			
CJ pressure	P_{cj}, GPa	21			

where γ is specific heat ratio, ρ is current density, ρ_0 is current density, e is initial internal energy. The bottom of the air mesh was assumed to have a perfectly reflecting boundary representing the ground, while the top and four sides of the air mesh were modeled as open spaces with transmitting boundaries. This ensured that the blast shock waves would be extinguished upon reaching these boundaries (Shin, 2014). For the computational domains (or boundary conditions) outside the tunnel entrance and exit, the entrance of the tunnel was defined as a transmitting boundary. This choice was based on the nature of detonation, which propagates radially from the center. Both transmitting and reflecting boundaries are valid in this context (Shin et al., 2014). The exit was set as a transmitting boundary to allow for the pressures to escape. This setting considered the scenario of a continuing tunnel, providing a realistic representation of how blast pressures would behave in an actual tunnel system.

The internal and external surfaces of the tunnel mesh were assumed to have perfectly reflecting boundaries, causing all surfaces to completely reflect the blast waves propagating through the air, resulting in complex effects such as reflection and diffraction (Fedorov et al., 2008; Shin et al., 2014; Skews et al., 2012). Modeling the tunnel as a rigid body ignores the interaction with structures, potentially leading to conservative calculations of blast overpressures reflected from the rigid structure. However, the differences in the results between rigid and deformable tunnels were deemed insignificant as the blast overpressures, calculated numerically under the assumption of rigid body structures, have been experimentally validated in numerous past studies (Denny et al., 2022; Shin et al., 2014; Shin et al., 2015a).

The simulation considered blast scenarios involving two TNT weights of 1000 and 2000 kg. The 1000-kg weight represents a substantial blast event, commonly considered in infrastructure protection and risk assessment studies (Han et al., 2010; Králik and Baran, 2013; Mandal et al., 2019; Mussa et al., 2020; Vaghefi and Mobaraki, 2021) for applications including underground tunnel, mining drift, and concrete bridge deck. This weight provides a baseline for understanding the impacts and mitigation strategies of significant blast loads. On the other hand, the 2000-kg weight was selected to examine the effects of an even large detonation, providing valuable data on the effectiveness of mitigation strategies under more extreme conditions. This dual-weight approach ensures that this study's outcomes are applicable and informative for a wide spectrum of scenarios, from substantial to severe, within the realm of explosive risk management.

Fig. 2 shows monitoring locations of overpressures and impulses in the tunnel, including an expansion chamber with a length-to-width ratio of 1.0. The detonation was initiated at the ground level on the left side of the straight tunnel with a length of 160 m. The ground-level detonations are typically considered in blast-resistant designs due to their real-world prevalence and relevance. While specific situations or theoretical considerations could include air-blast detonations, ground-level scenarios are more representative of actual risks and are therefore the focus of this study.

The expansion chamber was positioned 10 m away from the center of

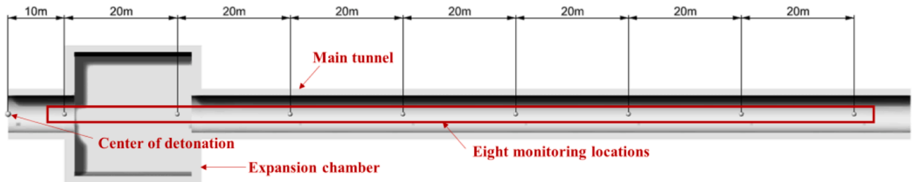

Fig. 2. Monitoring locations of overpressures and impulses from detonation.

detonation, aligning with an intermediate-field detonation level (scaled distance, Z, of 1.0 m/kg$^{1/3}$) for the 1000-kg baseline charge weight. This scaled distance, commonly used in blast-resistant design, balances near- and far-field ranges (Shin et al., 2014; Shin et al., 2015b). While varying this distance could impact the transition from a 3D spread to a 1D, planar wave form (Pennetier et al., 2015), this study focused on analyzing the shock wave behavior and chamber efficacy specifically at this distance. However, given the importance of the transition from 3D to 1D wave propagation for assessing overpressure and impulse reductions in the tunnel section following the chamber, this aspect was thoroughly evaluated in Section 3.2 to confirm its adequacy for facilitating the 1D wave propagation.

The blast overpressures were measured at eight monitoring locations spaced 20 m apart, starting from the point where the blast waves entered the expansion chamber. Through the CFD analysis, the behaviors of the blast overpressures at various distances and the effects of overpressure mitigation varying the design parameters of the expansion chamber were meticulously investigated.

3.2. Propagation laws of blast waves in tunnels

In confined spaces, such as tunnels, the characteristics of blast wave propagation differ markedly from those observed in free-field detonations. For free-field scenarios, various models have been proposed to describe the relationships between peak overpressures and distance, based on established free-field decay laws (Baker et al., 1983; Brode, 1959; Henrych and Major, 1979; Kingery and Bulmash, 1984; Mills, 1987). However, in confined spaces like tunnels, these free-field laws may significantly underestimate blast overpressures, as the blast energy is less likely to dissipate in such confined environments. Unlike the free-field scenario, confined detonations transition from a 3D spread to a 1D, planar wave form, altering the propagation pattern of the blast waves (Pennetier et al., 2015). Addressing this distinct propagation characteristic, Curran (1996) empirically developed a law for overpressure-distance relationships, specifically for peak overpressure ranging from 3.5 to 70 bar:

$$\frac{\Delta p}{p_0} = \left(\frac{M}{\Phi^2 R}\right)^{0.8} \tag{3}$$

where Δp is the blast overpressure, p_0 is the ambient pressure in undistributed medium ahead of the blast waves, M is the Mach number, Φ is the tunnel's cross-section diameter, R is the standoff distance from the center of detonation. Smith and Sapko (2005) proposed an alternate overpressure-distance law based on the Sachs' scaling principle, involving the overpressures ranges extending up to 0.4 bar:

$$\frac{\Delta p}{p_0} = 7.028\left(\frac{M}{AR}\right)^{0.514} \tag{4}$$

where A is the tunnel cross-sectional area. Silvestrini et al. (2009) introduced an overpressure-distance law that incorporates the concept of energy concentration:

$$\frac{\Delta p}{p_0} = 7.43538\left(\frac{M}{AR}\right)^{0.51} \tag{5}$$

Under the free-field law, blast waves are characterized by scaled distances. These include the Hopkinson-Cranz scaled distance Z, defined as $R/W^{1/3}$, where R is the standoff distance from the detonation center, and W is the charge weight. Alternatively, there is the Sachs scaled distance $\overline{R}$, defined as $R(p_0/E)^{1/3}$, used in ambient conditions that significantly deviate from sea level, where E is the explosive energy (Smith and Hetherington, 1994). For confined detonations, Silvestrini et al. devised a method to estimate the overpressures using the free-field laws, but with a modification of the scaled distances through an energy concentration factor (*ECF*). The *ECF*, a geometrical factor, is defined as the ratio of hemisphere volume (with a radius equal to current distance R), V_{hemi}, to the corresponding tunnel volume, V_{tunn}. In a normal tunnel scenario, V_{hemi} and V_{tunn} are calculated as $2\pi R^3/3$ and $2RA$, respectively. Thus, the *ECF* is defined as $\pi R^2/3A$. For confined spaces, the Hopkinson-Cranz Z is adapted to Z_c, calculated as $R/(ECF\ W)^{1/3}$, and for Sachs $\overline{R}$, it becomes $\overline{R}_c$, calculated as $R(p_0/(ECF\ E))^{1/3}$. These adaptions yield scaled-distance relationships between free-field and confined detonations, represented as Z_c/Z and $\overline{R}_c/\overline{R}$, both equating to $ECF^{1/3}$.

As the blast wave propagation pattern shifts from a free-field to a 1D form, the corresponding law governing overpressure decay changes as well. Prior to this transition, the decay of overpressure follows the free-field law. Once the transition occurs, the decay is more accurately represented by the 1D law, integrating the *ECF* concept. Benselama et al. (2010) introduced a scaled distance, Z_{TR}, to estimate the transition zone. This estimation takes into account the correlation between the discontinuity location and the relative diameter of the explosives:

$$Z_{TR} = \frac{0.0509}{(\alpha/100)^{13/9}} \tag{6}$$

where α is defined as $100d_c/d_H$, d_c is the charge diameter, d_H is the hydraulic diameter of tunnel ($=4A/L_p$), and L_p is the perimeter of the cross-section.

Considering the tunnel shape shown in Fig. 1(b) and a charge weight of 1000 kg, α for this tunnel cross-section is determined to be 16.97. This calculation leads to Z_{TR} of 0.66 m/kg$^{1/3}$, indicating that the blast waves would transition to the 1D law after traveling 6.6 m from the detonation point. This distance was regarded as the minimum required for overpressure stabilization within the tunnel. The primary location for monitoring overpressure mitigation, the central focus of this study, is positioned 150 m from the detonation point. As the blast waves pass through the expansion chamber and re-enter the main tunnel, they initially exhibit 3D behavior due to the corner diffraction and subsequent reflections at the inlet, but gradually transition to a stabilized, 1D planar wave form. Given that the distance from the inlet to the 150-m location was 116 m, the length of the tunnel following the chamber was deemed sufficient for achieving stabilized overpressures. This holds true for all other tunnel configurations in established blast scenarios (see Section 4.1 for details).

3.3. Mesh sensitivity analysis

A mesh sensitivity study was performed using the baseline model, as shown in Fig. 1(a), for a charge weight, W, of 1000 kg of TNT to ensure the numerical accuracy and computational efficiency. Three mesh sizes of 0.1, 0.2 and 0.4 m were considered based on Shin and Pang (2022). The blast overpressures were measured at eight locations, as shown in

Fig. 2. The results of the mesh sensitivity analysis are presented in Fig. 3. As the standoff distance, R, increases, the mesh convergence with respect to the maximum overpressure, P_M, was significantly improved. Across all distances, the mesh sizes of 0.1 and 0.2 m exhibited minimal variation compared with those of 0.2 and 0.4 m. For the 0.1-m mesh size, the overpressure peaked at 808 kPa at R = 10 m and diminished to 77 kPa at R = 150 m.

In examining the dynamics of wave propagation within the tunnel, it is important to consider the spatial constraints imposed by the tunnel's dimensions. Since the 1D analysis results conducted up to 9 m were remapped into a 3D domain for further analysis, no effects of reflection and diffraction were considered up to this point. This was because the primary purpose was to generate to generate specific shockwaves prior to entering the expansion chamber, focusing on assessment of the overpressure mitigation effects of the expansion chamber. Also, since these shockwaves were expected to adhere to the free-field law, this enabled validation of the results at 10 m using empirical blast load design charts in UFC 3–340-02 (DoD, 2008), as presented in Section 3.4. Further, at R = 150 m, used primarily for overpressure mitigation, sufficient consideration was given to ensure the formation of a 1D wave propagation pattern, as described previously in Section 3.2.

In Fig. 3(a), the 1D to 3D remapping approach allows to interpret the overpressure history measured at 10 m. Between approximately 0.005 and 0.008 sec, the overpressure behavior can be considered consistent with the propagation following the 3D, free-field law, as described in Section 3.2. However, the peaks around approximately 0.009 and 0.011 sec are indeed indicative of more complex phenomena, likely due to reflections off the tunnel's internal walls and diffraction at the chamber entrance. These multidimensional effects are evident in the overpressure history at 10 m and highlight the complex dynamics of blast waves in confined spaces.

Fig. 4(a) shows P_M in relation to R for W = 1000 kg. Mesh convergence was considered achieved when the results obtained using a cell size reduced by a factor of two change by 10 % or less. The discrepancy between the results for mesh sizes of 0.2 and 0.4 m exceeded 10 % at R = 10 and 30 m. For mesh sizes of 0.1 and 0.2 m, all results met the 10 % limit. Based on the results of the mesh sensitivity analysis, it can be firmly concluded that mesh sizes ranging 0.1 to 0.2 m yield mesh-converged solutions for the tunnel analysis model.

3.4. Numerical validation

The overpressure histories, calculated from the mesh sensitivity study at R = 10 m for W = 1000 kg and the cell sizes of 0.1 and 0.05 m, were compared to the estimations derived from the design charts available in UFC 3–340-02 (DoD, 2008), as shown in Fig. 5. This estimation was based on the Friedlander curve (Hetherington and Smith, 1994). The scaled distance, Z, was set at 1.0 m/kg$^{1/3}$. The CFD calculations led to P_M of 870 kPa for the 0.1 m cells and 942 kPa for 0.05 m, while the UFC 3–340-02 prediction was 940 kPa, showing a minor discrepancy of −7.4 % and 0.02 %, respectively. A divergence in the overpressure histories occurred after approximately t = 8 ms, likely attributed to the repeated reflection of the blast waves by the interior tunnel walls. Given the comprehensive assessment of the overpressure stability evaluation, mesh sensitivity and numerical validation, the established numerical model was considered validated.

While the overpressure history at a distance of R = 10 m showed a minor discrepancy with empirical data, extending this validation to other monitoring locations (R = 30 m to 150 m) presented challenges. These distances involved complex overpressure behaviors influenced by multiple reflections and diffractions from interior tunnel walls, making direct empirical validation against sources like UFC 3–340-02 less straightforward. However, it is crucial to recognize that the robust foundation and extensive validation of the Viper::Blast tool. Developed based on the seminal works by Rose (2010) and Wada and Liou (1994), it has been a preferred tool in various blast-related studies, including Marks et al. (2021), Angelides et al. (2023), and Dennis et al. (2023a). These studies, along with others such as Kalubadanage et al. (2020), Angelides et al. (2022), and Dennis and Rigby (2023), have extensively validated the accuracy of the numerical algorithms in computing overpressure and impulse across a wide range of scaled distances. This extensive body of validation gives confidence in the reliability of the numerically calculated results. It is important to note that this confidence is contingent upon achieving mesh convergence at all monitoring locations and empirically validating the results at least at one location, considering the variations in results that may depend on specific blast input parameters.

4. Computational fluid dynamics analysis

4.1. Blast scenario

The impact of overpressure reduction in a protective tunnel, depending on the design of expansion chamber, were investigated using CFD analysis with the numerical model validated in Section 3. For this purpose, blast scenarios were established in consideration of the design parameters of the chamber and detonation. The blast scenarios were divided into two groups varying charge weights: 1000 kg (Group (1) and 2000 kg (Group (2). The simulation matrix for Group (1) was composed of twenty-five models, as presented in Table 2. The baseline model, designated as G1-0, was designed without the chamber, which is shown in Fig. 1(a). The effects of overpressure and impulse mitigation of the models with the chamber were evaluated based on the model G1-0.

Models G1-25 to G1-400 were made to examine the effect of the length-to-width ratio of the chamber (L_c/W_c), ranging from 0.25 to 4.0. The model G1-100, with L_c/W_c of 1.0, is shown in Fig. 1(b). Models G1-50–14.9 to G1-400–14.9 were made by increasing the chamber heights, H_c, of models G1-50 to G1-400 from 8 to 14.9 m to look into the height effect of the chamber. The last seven models G1-W12 to G1-W109 were prepared to observe the effect of the chamber width, W_c, which ranged

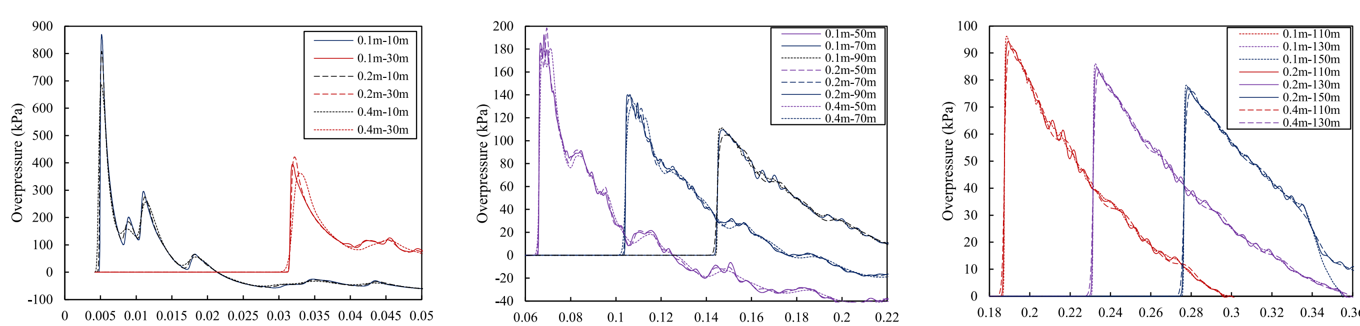

(a) R = 10 m, 30 m (b) R = 50 m, 70 m, 90 m (c) R = 110 m, 130 m, 150 m

Fig. 3. Overpressure histories as a function of distance for W = 1000 kg.

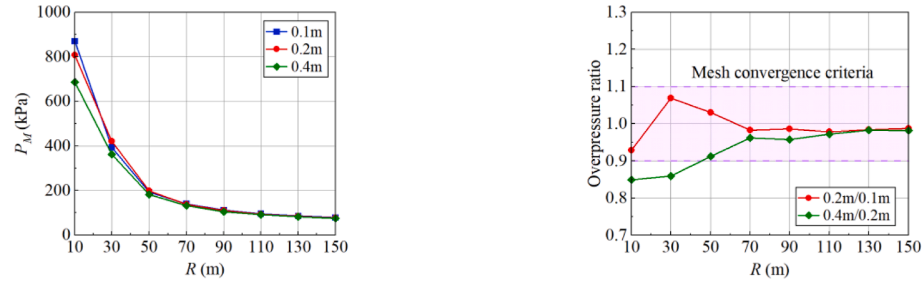

(a) P_M vs R (b) Normalized P_M

Fig. 4. Differences in P_M varying cell sizes of 0.1, 0.2 and 0.4 m for $W = 1000$ kg.

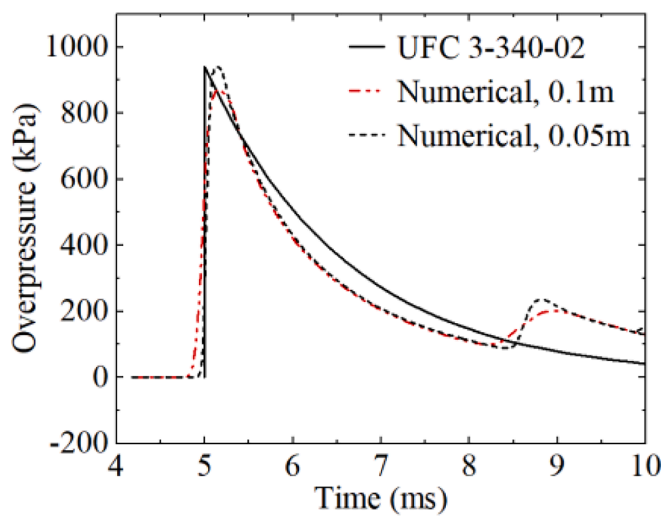

Fig. 5. Overpressure histories between UFC 3–340-02 prediction and CFD calculations with different cell sizes.

1.2 to 10.9. The simulation matrix for Group (2) was made similar to that for Group (1). The primary distinction between the models in Groups (1) and (2) was the charge weight. In the model identifiers (ID), the designation “G1” representing Group (1) was replaced with “G2” for Group (2).

The physical quantities of variables (L_c/W_c, W_c/W_t, and H_c) by models are illustrated in Fig. 6. These variables are identified as key factors that significantly influence the reduction of overpressures. The chamber length-to-width ratio (L_c/W_c) is a measure of the relative length to width of the expansion chamber. It reflects how elongated the chamber is in comparison to its width, which is an essential factor in determining the chamber’s capacity to dissipate the energy of a blast wave. The chamber-to-tunnel width ratio (W_c/W_t) compares the width of the expansion chamber to the overall width of the tunnel. It indicates how much of the tunnel’s cross-sectional area is occupied by the chamber, which is crucial for understanding the chamber’s impact on the flow and behavior of blast waves within the tunnel. The chamber height (H_c) represents the vertical dimension of the expansion chamber. The height of the chamber is a critical component in assessing the volume available for blast wave energy dissipation and is directly linked to the chamber’s effectiveness in reducing overpressures.

4.2. *Blast wave propagation in tunnel with expansion chamber*

The behavior of blast wave propagation was observed by examining the overpressure distribution in the expansion chamber-installed tunnel at the bottom level for models G1-0 and G1-100. For these models, the 1D analyses were conducted until the shockwaves traveled 9 m before

Table 2
Simulation matrix for expansion chamber; Group (1).

No.	Model ID	Expansion chamber			L_c/W_c	W_c/W_t	Note
		L_c (m)	W_c (m)	H_c (m)			
1	G1-0	No expansion chamber			–	–	Baseline model
2	G1-25	6.1	24.3	8.0	0.25	2.7	First subset
3	G1-50	12.2	24.3	8.0	0.5	2.7	comprising models
4	G1-100	24.3	24.3	8.0	1.0	2.7	varying L_c (and $L_c/$
5	G1-150	36.5	24.3	8.0	1.5	2.7	W_c L_c/W_c) compared
6	G1-200	48.6	24.3	8.0	2.0	2.7	to the baseline (G1-
7	G1-250	60.8	24.3	8.0	2.5	2.7	0)
8	G1-300	72.9	24.3	8.0	3.0	2.7	
9	G1-350	85.1	24.3	8.0	3.5	2.7	
10	G1-400	97.2	24.3	8.0	4.0	2.7	
11	G1-50–14.9	12.2	24.3	14.9	0.5	2.7	Second subset
							comprising models
12	G1-100–14.9	24.3	24.3	14.9	1.0	2.7	increasing H_c from 8.0 m to 14.9 m
13	G1-150–14.9	36.5	24.3	14.9	1.5	2.7	from the first subset models
14	G1-200–14.9	48.6	24.3	14.9	2.0	2.7	
15	G1-250–14.9	60.8	24.3	14.9	2.5	2.7	
16	G1-300–14.9	72.9	24.3	14.9	3.0	2.7	
17	G1-350–14.9	85.1	24.3	14.9	3.5	2.7	
18	G1-400–14.9	97.2	24.3	14.9	4.0	2.7	
19	G1-W12	24.3	10.7	8.0	2.28	1.2	Third subset
20	G1-W15	24.3	13.4	8.0	1.82	1.5	comprising models
21	G1-W20	24.3	17.8	8.0	1.37	2.0	varying W_c (and $W_c/$
22	G1-W27	24.3	24.3	8.0	1.00	2.7	W_t) compared to the
23	G1-W40	24.3	35.6	8.0	0.68	4.0	baseline (G1-0)
24	G1-W55	24.3	48.6	8.0	0.50	5.5	
25	G1-W109	24.3	97.2	8.0	0.25	10.9	

the blast waves entered the chamber. This specific range was chosen due to the expansion chamber being located 10 m from the detonation point, allowing analysis of wave propagation just prior to its interaction with the chamber. Furthermore, this decision optimized computational resources and efficiency. These 1D data were then mapped into the 3D domain, as shown in Fig. 7(a) and 7(g) for models G1-0 and G1-100, respectively, representing the initial state of the 3D analyses. The propagation of the blast waves in tunnels is characterized by a sequence of shockwave reflections and mergers. In the baseline model (G1-0), the shockwaves were initially reflected off the internal walls as they advance forward, as shown in Fig. 7(b). The shock front of the incident waves was followed by the reflected waves. These waves eventually merged into a single wavefront when the reflected waves caught up with the incident waves, as shown in Fig. 7(c). This figure shows the process where the reflected overpressures were re-reflected. Subsequently, these re-reflected overpressures merged back with the waves at the shock

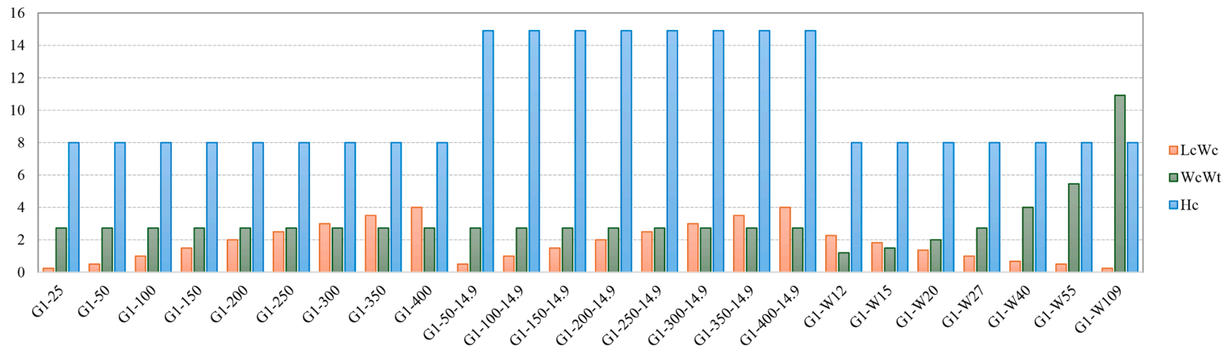

Fig. 6. Comparison of physical quantities of expansion chamber variables.

front, as shown in Fig. 7(d). This pattern of repeated reflection and merging at the shock front resulted in the generation of third- and fourth-order reflected overpressures, which are demonstrated in Fig. 7 (d) and 7(e).

For model G1-100, the 3D analysis commenced at $t = 4$ ms, similar to the model G1-0. This corresponds to when the shock front of the incident waves reaches 9 m, as shown in Fig. 7(g). When the shockwaves entered the chamber, those propagating along the walls experienced diffraction at the corner, resulting in the formation of vortices radiating outwards, as shown in Fig. 7(h). Eventually, the incident and diffracted waves merged, forming a new shock front, as shown in Fig. 7(i). The diffracted shockwaves were then reflected off the side walls of the chamber, creating a Mach stem (Bai et al., 2022) by combining the diffracted and reflected waves, as shown in Fig. 7(j).

At $t = 49$ ms (Fig. 7(k)), the shock front entered the main tunnel from the chamber. The shock front velocity of model G1-100 was slightly slower than that of model G1-0, as shown in Fig. 7(e) and 7(k), noting that the propagation distances of the two models at this point were approximately 37 and 40 m, respectively, and the magnitude at the shock front was consequently smaller for model G1-100. These differences were attributed to the diffracted waves for model G1-10.

At $t = 84$ ms, the ongoing reflection and diffraction of the remaining shock waves in the chamber were observed while the shock fronts moving forward in the main tunnel, as shown in Fig. 7(l). The quantitative effect of the chamber on overpressure and impulse mitigation in the protective tunnel is discussed later in this paper.

4.3. Results for maximum overpressures, P_M

The results of overpressure histories for $W = 1000$ kg are presented in Fig. 8. All models exhibited a consistent trend: the maximum overpressures (P_M) decrease with increasing distance (R), as expected. Using the expansion chamber significantly reduced overpressures compared to the results for model G1-0. The fluctuation in the overpressure histories was a consequence of the repeated shockwave reflections and diffractions inside the chamber. The P_M turned out to be captured at the initial few peaks in the overpressure histories. For instance, the P_M for model G1-50 at $R = 30$ m was observed at the first peak (approximately $t = 0.04$ s), whereas for model G1-100 and the same distance, the P_M was captured at the second peak (approximately $t = 0.07$ s), as shown in Fig. 8(c) and 8(d), respectively. Such observations were consistent across all other models.

The results of P_M for $W = 1000$ kg are summarized in Table 3. For the first subset (G1-25 to G1-400), the P_M reductions at $R = 150$ m ranged from 27 % to 52 %, with the greatest reduction of 52 % for model G1-300. For the second subset (models G1-50–14.9 to G1-400–14.9 with increased chamber heights of 14.9 m), the reductions ranged from 54 % to 64 %. This indicates a 1.23-fold improvement as the chamber height increased. This observation highlights some influence of chamber height on overpressure reduction. For the last subset of models (G1-W12 to G1-W109), designed to probe the effect of chamber width, the reductions ranged from 9 % to 63 %, with the most significant reductions of 63 % observed in the last three models (G1-W40, G1-W55 and G1-W109). This suggests that the overpressure reduction effects were most significant when the chamber-to-tunnel width ratios, W_c/W_t, were 4.0 or greater.

The observations for Group (1) were similar to those for Group (2), for which the results are presented in Table 4. For the first subset (G2-25 to G2-400), the P_M reductions ranged from 28 % to 52 %. The reductions for the second subset (G2-50–14.9 to G2-400–14.9) ranged from 52 % to 61 %, showing a 1.17-fold enhancement with the increased chamber heights. The reductions for the last subset (G2-W12 to G2-W109) ranged from 22 % to 66 %, with the most significant reductions of 64 % to 66 % observed in the last three models.

The study on blast overpressure mitigation in a tunnel demonstrates a clear trend: maximum overpressure decreases with distance. Significantly, using an expansion chamber greatly reduces overpressures compared to the baseline model. The study highlights the importance of chamber geometry, with both chamber height and width playing crucial roles in mitigating overpressures. Larger chamber-to-tunnel width ratios are particularly effective, indicating the potential for tailored design in reduction systems of blast overpressure to enhance safety and efficiency.

4.4. Results for maximum impulse, I_M

The impulse histories were derived by integrating the overpressure histories over time. The results for Group (1), calculated from the overpressure data shown in Fig. 8, are presented in Fig. 9. Regarding the first subset (G1-25 to G1-400), the maximum impulses (I_M) for G1-0 and G1-25 tended to increase rather than decrease with distance, whereas for other models, the I_M at $R = 150$ m decreased compared to those at $R = 10$ m, as shown in Fig. 9(a) to 9(j). In the second subset (G1-50–14.9 to G1-400–14.9), all models showed a decrease in I_M at $R = 150$ m, as shown in Fig. 9(k) to 9(r). The trend observed in the third subset (G1-W12 to G1-W109) was comparable to that for the first subset, as shown in Fig. 9(s) to 9(y). It should be noted that none of the maximum impulses were greater than that of the baseline model (G1-0).

Table 5 summarizes the results of I_M for Group (1). Similar to the observations for P_M, the effect of reduction for I_M was assessed at $R = 150$ m. In the first subset (G1-25 to G1-400), the reductions in I_M ranged from 25 % to 53 %. This range is comparable to that of P_M, with the most significant reduction of 53 % observed for model G1-350. In the second subset (G1-50–14.9 to G1-400–14.9), the reductions ranged from 54 % to 66 %. This pattern of reduction aligns closely with that observed for P_M. Model G1-250–14.9 exhibited the greatest reduction of 66 %. When the chamber height increased to 14.9 m, the reduction increased by a factor of 1.22 from 54 % to 66 %, indicating a noticeable effect of height on impulse reduction, similar to the results for P_M. For the third subset (G1-W12 to G1-W109), the I_M reductions spanned from 12 % to 73 %. The most pronounced reduction (73 %) was for the last model, G1-

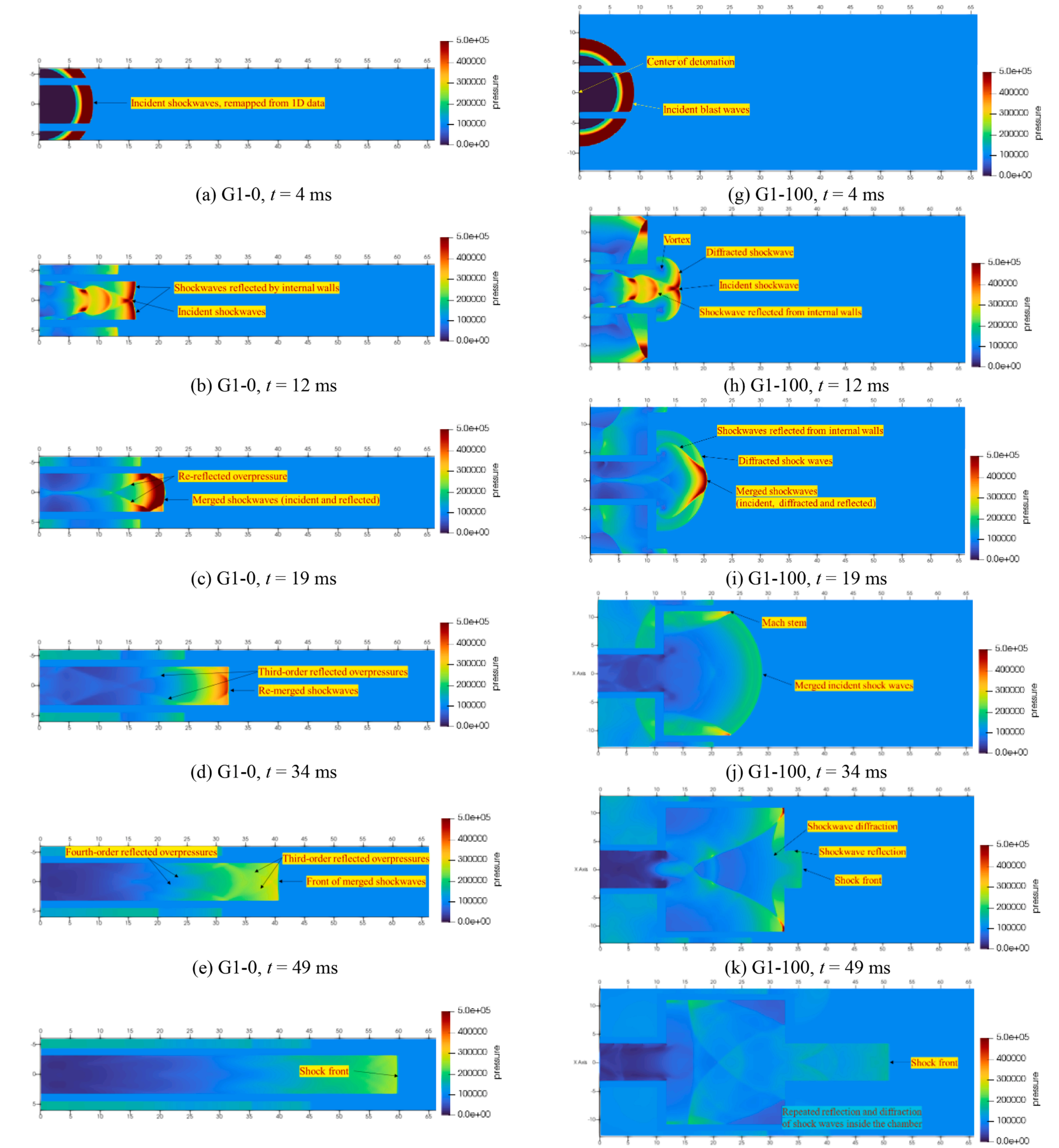

(a) G1-0, t = 4 ms (b) G1-0, t = 12 ms (c) G1-0, t = 19 ms (d) G1-0, t = 34 ms (e) G1-0, t = 49 ms (f) G1-0, t = 84 ms (g) G1-100, t = 4 ms (h) G1-100, t = 12 ms (i) G1-100, t = 19 ms (j) G1-100, t = 34 ms (k) G1-100, t = 49 ms (l) G1-100, t = 84 ms

Fig. 7. Shockwave propagation in tunnel.

W109.

Table 6 presents the results for Group (2). The observations for Group (1) were consistent with those for Group (2). For models G2-25 to G2-400, the I_M reductions varied from 12 % to 48 %. In models G2-50–14.9 to G2-400–14.9, the reductions ranged from 34 % to 63 %, marking a 1.31-fold enhancement as the height increased from 8.0 to 14.9 m. For models G2-W12 to G2-W109, the reductions ranged from 12 % to 57 %, with the most significant reductions of 49 % to 57 % observed in the last two models of G2-W55 and G2-W109.

These results provide a general insight into the behavior of impulses resulting from detonation. It reveals that the impulse response to detonations is not always linear with respect to distance or model configuration. While some models show an increase in impulse with distance, others exhibit a decrease, highlighting the complexity of shockwave behaviors. The significant impact of chamber geometry on impulse reduction is a key finding. Both increased chamber height and width are

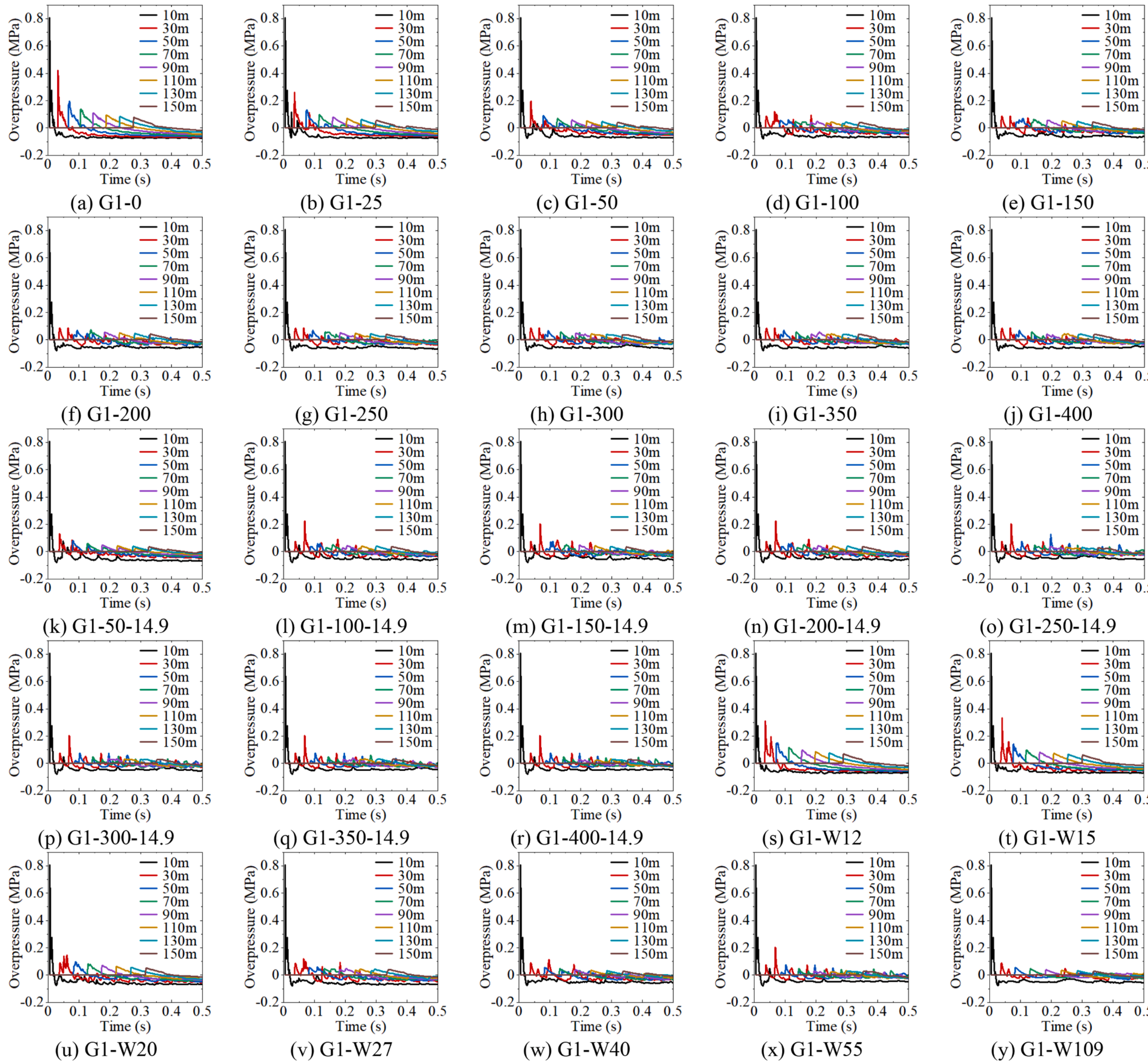

Fig. 8. Overpressure histories for $W = 1000$ kg; Group (1).

shown to effectively reduce impulses, suggesting that optimizing chamber dimensions could be a crucial strategy in designing explosion containment systems. This observation underscores the importance of tailored design in controlling the blast forces, offering a broader perspective for safety and efficiency in handling blast scenarios.

5. Effects of expansion chamber on overpressures and impulses

The effects of the expansion chamber on the reduction in the maximum overpressure (P_M) and impulse (I_M) are discussed in more detail in this section. This discussion focused on the effects of the chamber's length-to-width ratio (L_c/W_c), chamber-to-tunnel width ratio (W_c/W_t), chamber height (H_c), and charge weight (W).

5.1. Maximum overpressure, P_M, as a function of L_c/W_c

A concept of overpressure stability was considered in the terms of the blast wave propagation behavior. Fig. 10 shows the relationship between P_M and R for $W = 1000$ kg and reveals a pattern where the P_M values decrease along a curve with increasing R. Specifically, as the L_c/W_c ratio of the expansion chamber increases, the P_M at each observation R decreases until it reaches a point where further increases in the L_c/W_c ratio do not significantly reduce the P_M. This phenomenon is visually represented as a downward convergence of the overpressure-distance curve with increasing L_c/W_c ratios. This convergence (or stabilization) point of overpressure was defined as overpressure stability. In Fig. 10, it is evident that the P_M consistently decreased with increasing R across all models. In the first subset ($H_c = 8.0$ m), the decrease in P_M with R was steeper for greater L_c/W_c. Moreover, the P_M - R curves were inclined to converge when the L_c/W_c L_c/W_c was 1.0 or greater, as shown in Fig. 10 (a). For the second subset ($H_c = 14.9$ m), all P_M-R curves appeared nearly identical, as shown in Fig. 10(b), indicating that the chamber height contributes to the reduction and stabilization of overpressure. This can be explained by the fact that in the first subset models, the diffractions occurred solely from the side-wall edges, while additional diffractions from the upper edges for the second subset arose, leading to further overpressure reduction. These observations were essentially identical for Group (2), as shown in Fig. 11.

Table 3
P_M for $W = 1000$ kg; Group (1).

No.	Model ID	Maximum overpressures, P_M (kPa)								Red. (%) (150 m)
		10 *m*	30 *m*	50 *m*	70 *m*	90 *m*	110 *m*	130 *m*	150 *m*	
1	G1-0	808	421	197	138	110	94	85	77	0
2	G1-25	808	261	132	97	79	69	62	57	27 %
3	G1-50	808	195	90	68	58	51	46	42	46 %
4	G1-100	808	119	60	47	46	43	42	41	47 %
5	G1-150	808	87	70	63	55	52	48	43	44 %
6	G1-200	808	87	68	75	57	49	46	42	45 %
7	G1-250	808	85	68	57	52	48	43	40	48 %
8	G1-300	808	87	68	57	49	43	40	37	52 %
9	G1-350	808	85	68	57	58	44	41	40	48 %
10	G1-400	808	85	68	57	42	43	42	40	48 %
11	G1-50–14.9	808	132	80	59	49	43	39	35	54 %
12	G1-100–14.9	808	224	60	50	44	42	39	38	51 %
13	G1-150–14.9	808	203	73	51	48	42	37	34	56 %
14	G1-200–14.9	808	224	60	50	44	42	39	38	51 %
15	G1-250–14.9	808	203	128	49	37	33	31	28	64 %
16	G1-300–14.9	808	203	74	52	34	30	29	29	62 %
17	G1-350–14.9	808	203	74	60	39	34	32	31	60 %
18	G1-400–14.9	808	203	74	49	30	33	31	30	61 %
19	G1-W12	808	310	152	117	96	85	77	70	9 %
20	G1-W15	808	334	142	97	82	73	67	61	21 %
21	G1-W20	808	147	98	83	72	64	57	52	33 %
22	G1-W27	808	119	60	47	46	43	42	41	47 %
23	G1-W40	808	114	54	46	39	34	31	29	63 %
24	G1-W55	808	90	54	46	39	35	31	29	63 %
25	G1-W109	808	88	54	46	39	35	31	29	63 %

Table 4
P_M for $W = 2000$ kg; Group (2).

No.	Model ID	Maximum overpressures, P_M (kPa)								Red. (%)
		10 *m*	30 *m*	50 *m*	70 *m*	90 *m*	110 *m*	130 *m*	150 *m*	
1	G2-0	1436	902	383	260	184	154	137	125	0
2	G2-25	1436	526	266	166	130	110	98	90	28 %
3	G2-50	1436	421	155	115	92	80	72	65	48 %
4	G2-100	1436	241	147	92	96	84	78	72	43 %
5	G2-150	1436	182	129	106	93	83	75	69	45 %
6	G2-200	1436	167	117	124	87	79	70	65	48 %
7	G2-250	1436	161	119	98	81	73	67	61	52 %
8	G2-300	1436	167	117	90	80	66	66	66	48 %
9	G2-350	1436	161	118	90	112	71	69	67	46 %
10	G2-400	1436	161	118	105	63	69	67	64	49 %
11	G2-50–14.9	1436	259	137	100	79	68	60	57	55 %
12	G2-100–14.9	1436	336	116	91	85	74	66	60	52 %
13	G2-150–14.9	1436	250	124	96	75	67	60	53	58 %
14	G2-200–14.9	1436	250	145	86	71	59	51	47	63 %
15	G2-250–14.9	1436	250	129	90	60	56	53	54	57 %
16	G2-300–14.9	1436	250	129	92	63	58	56	56	55 %
17	G2-350–14.9	1436	250	129	116	75	58	55	52	58 %
18	G2-400–14.9	1436	250	129	75	58	55	48	49	61 %
19	G2-W12	1396	897	384	258	183	152	136	125	0 %
20	G2-W15	1396	651	287	167	133	116	106	97	22 %
21	G2-W20	1396	265	189	140	116	100	90	81	36 %
22	G2-W27	1393	254	149	94	95	85	79	72	42 %
23	G2-W40	1396	205	87	71	60	52	48	45	64 %
24	G2-W55	1391	162	87	72	60	53	47	43	66 %
25	G2-W109	1394	160	88	72	60	53	47	43	66 %

The relationships between P_M at $R = 150$ m and L_c/W_c for the first two subsets ($H_c = 8.0$ and 14.9 m) of Groups (1) and (2) ($W = 1000$ and 2000 kg, respectively) are presented in Fig. 12(a). For all cases, there was no significant overpressure reduction when L_c/W_c was larger than 0.5. The P_M for $W = 1000$ kg decreased from 77 to 40 kPa for $H_c = 8.0$ and to 30 kPa for $H_c = 14.9$ m. For $W = 2000$ kg, the P_M diminished from 125 to 64 and 49 kPa, respectively.

Fig. 12(b) shows the results of the P_M reduction at $R = 150$ m as a function of L_c/W_c L_c/W_c. The reductions appeared virtually consistent for each chamber height, irrespective of charge weight. With $H_c = 8.0$ and 14.9 m, the P_M reductions averaged 48 % and 58 %, respectively, indicating that on average, increasing the chamber height from 8.0 to 14.9 m resulted in a 21 % improvement in the overpressure reduction. The main reason for this reduction was the behavior of shock waves as they entered the expansion chamber from the main tunnel. At this point, the maximum overpressures at the shock front diminished due to the upward dispersion of the blast waves, driven by the diffraction effect from the upper edge, as shown in Fig. 13, which captures the shock wave propagations at $t = 33$ and 66 ms for models G1-400 (with $H_c = 8.0$ m) and G1-400–14.9 (with $H_c = 14.9$ m).

In addressing the observed consistency in overpressure reduction rates across different chamber heights and irrespective of explosive

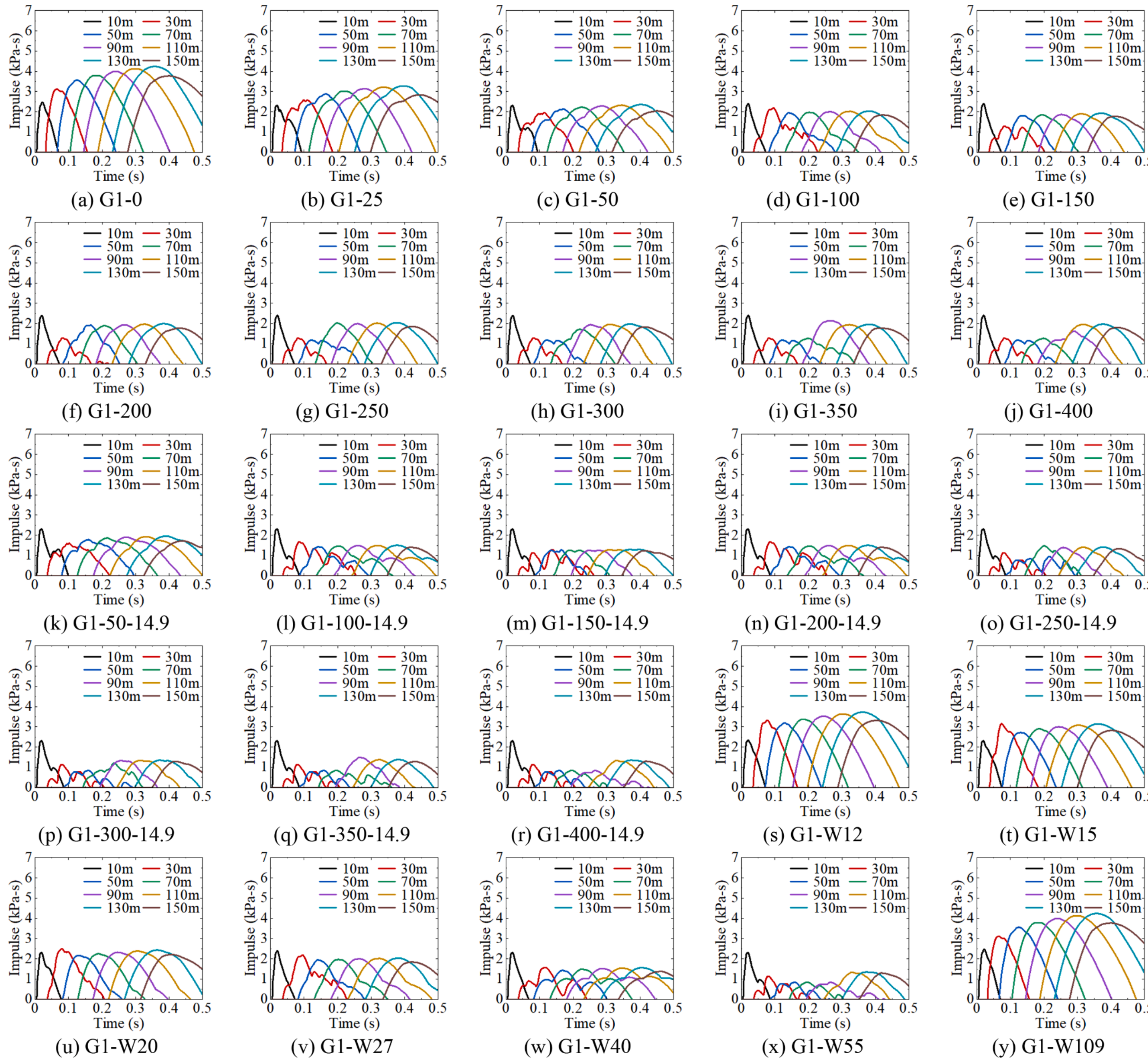

Fig. 9. Impulse histories for $W = 1000$ kg; Group (1).

charge weights in this numerical study, it's crucial to consider the interplay of chamber design and shockwave dynamics. The expansion chamber's design, particularly its height, plays a pivotal role in absorbing and diffusing shockwaves. A taller chamber provides increased space for the shockwave to expand, allowing for more effective energy dissipation, which can result in comparable overpressure reduction percentages despite varying initial energies from different explosive weights. Furthermore, the height influences diffraction patterns, with taller chambers inducing more diffraction and scattering of shockwaves due to additional surfaces like upper edges, leading to more pronounced overpressure reductions. These effects are consistent across different explosive weights, as they are more reliant on the chamber's geometry than on the explosive force itself. Additionally, it's important to acknowledge the potential limitations and specific conditions of our numerical models, which might also contribute to these consistent findings. Overall, the effectiveness of the chamber's design, especially in terms of height, is critical in managing shockwave dynamics and energy dissipation, rendering the initial magnitude of the explosion less impactful compared to the geometry and internal dynamics of the chamber.

The study presented in this section highlights a crucial relationship between chamber geometry and overpressure reduction in blast environments. It shows that maximum overpressure (P_M) decreases with increased distance from the detonation. Significantly, steeper P_M reductions are observed in chambers with higher length-to-width ratios (L_c/W_c). Additionally, increased chamber height, as seen in the nearly identical P_M -R curves for 14.9 m high chambers, plays a pivotal role in stabilizing and reducing overpressures. These suggest that optimizing chamber dimensions, particularly height, is key to more effective blast wave mitigation, offering valuable guidance for designing safer blast mitigation systems.

5.2. Maximum impulse, I_M, as a function of L_c/W_c

The maximum impulses (I_M) as a function of distance (R) calculated for the first subset of Group (1) ($H_c = 8.0$ m and $W = 1000$ kg) are presented in Fig. 14(a). For the model G1-0, the I_M tended to rise with increasing R. The model G1-25 displayed a similar trend, though the

Table 5
I_M for $W = 1000$ kg; Group (1).

No.	Model ID	Maximum impulse, I_M (kPa-s)								Red. (%)
		10 *m*	30 *m*	50 *m*	70 *m*	90 *m*	110 *m*	130 *m*	150 *m*	
1	G1-0	2.5	3.1	3.6	3.8	4.0	4.1	4.2	3.8	0
2	G1-25	2.3	2.6	2.9	3.0	3.1	3.2	3.3	2.8	25 %
3	G1-50	2.3	2.0	2.1	2.2	2.3	2.3	2.4	2.0	46 %
4	G1-100	2.4	2.2	1.9	2.0	2.0	2.0	2.0	1.8	51 %
5	G1-150	2.4	1.3	1.8	1.8	1.9	1.9	1.9	1.8	53 %
6	G1-200	2.4	1.3	1.9	1.9	1.9	2.0	2.0	1.8	53 %
7	G1-250	2.4	1.3	1.2	2.0	2.0	2.0	2.0	1.9	51 %
8	G1-300	2.4	1.3	1.2	1.7	1.9	2.0	2.0	1.8	51 %
9	G1-350	2.4	1.3	1.2	1.3	2.1	1.9	2.0	1.8	53 %
10	G1-400	2.4	1.3	1.2	1.3	1.6	2.0	2.0	1.8	52 %
11	G1-50–14.9	2.3	1.6	1.8	1.9	1.9	1.9	2.0	1.7	54 %
12	G1-100–14.9	2.3	1.7	1.4	1.5	1.5	1.5	1.5	1.4	63 %
13	G1-150–14.9	2.3	1.3	1.3	1.3	1.3	1.3	1.3	1.2	67 %
14	G1-200–14.9	2.3	1.7	1.4	1.5	1.5	1.5	1.5	1.4	63 %
15	G1-250–14.9	2.3	1.1	1.0	1.5	1.4	1.4	1.4	1.3	65 %
16	G1-300–14.9	2.3	1.1	0.8	1.2	1.3	1.3	1.4	1.3	66 %
17	G1-350–14.9	2.3	1.1	0.8	0.8	1.5	1.4	1.4	1.3	66 %
18	G1-400–14.9	2.3	1.1	0.8	0.8	0.8	1.3	1.4	1.3	66 %
19	G1-W12	2.3	3.3	3.2	3.4	3.5	3.6	3.7	3.3	12 %
20	G1-W15	2.3	3.2	2.7	2.9	3.0	3.1	3.1	2.8	25 %
21	G1-W20	2.3	2.5	2.2	2.3	2.3	2.4	2.4	2.2	41 %
22	G1-W27	2.4	2.2	1.9	2.0	2.0	2.0	2.0	1.8	51 %
23	G1-W40	2.3	1.6	1.4	1.5	1.5	1.5	1.6	1.4	63 %
24	G1-W55	2.3	1.1	0.8	0.8	0.8	1.3	1.4	1.3	66 %
25	G1-W109	2.3	0.9	1.0	1.0	1.0	1.1	1.1	1.0	73 %

Table 6
I_M for $W = 2000$ kg; Group (2).

No.	Model ID	Maximum impulse, I_M (kPa-s)								Red. (%)
		10 *m*	30 *m*	50 *m*	70 *m*	90 *m*	110 *m*	130 *m*	150 *m*	
1	G2-0	5.0	5.5	6.0	6.5	6.9	7.2	7.5	6.7	0
2	G2-25	5.9	5.4	6.0	6.3	6.6	6.7	6.9	6.0	12 %
3	G2-50	5.6	5.0	5.3	5.5	5.6	5.8	5.8	5.0	27 %
4	G2-100	5.3	5.3	4.4	4.6	4.7	4.7	4.6	4.2	38 %
5	G2-150	5.1	4.3	4.1	4.3	4.4	4.5	4.0	3.9	43 %
6	G2-200	4.8	4.1	4.7	4.1	4.3	4.1	4.1	3.8	43 %
7	G2-250	4.3	4.0	3.8	3.9	3.9	4.0	4.1	3.5	48 %
8	G2-300	4.3	3.7	3.6	4.2	3.9	4.0	4.0	3.5	48 %
9	G2-350	4.3	3.4	3.4	3.9	4.7	4.0	4.0	3.5	48 %
10	G2-400	4.3	3.2	3.2	3.7	4.2	3.9	4.0	3.5	48 %
11	G2-50–14.9	5.5	4.5	4.9	5.1	5.2	5.3	5.1	4.4	34 %
12	G2-100–14.9	5.3	4.6	4.1	4.3	4.4	4.3	4.0	3.6	46 %
13	G2-150–14.9	5.2	3.7	3.5	3.6	3.8	3.9	3.2	2.6	61 %
14	G2-200–14.9	4.9	3.3	4.0	3.4	3.5	3.0	2.9	2.6	62 %
15	G2-250–14.9	4.5	2.9	3.3	3.3	2.8	2.8	2.9	2.5	63 %
16	G2-300–14.9	4.3	2.8	2.8	3.1	2.8	2.8	2.8	2.5	63 %
17	G2-350–14.9	4.3	2.5	2.5	2.9	3.3	2.8	2.8	2.5	63 %
18	G2-400–14.9	4.3	2.0	2.4	2.7	2.9	2.8	2.8	2.5	63 %
19	G2-W12	5.5	6.4	5.5	5.9	6.3	6.5	6.7	6.0	12 %
20	G2-W15	5.8	6.0	4.8	5.2	5.5	5.6	5.8	5.1	24 %
21	G2-W20	5.9	5.2	4.4	4.7	4.9	5.0	4.9	4.5	34 %
22	G2-W27	5.2	5.2	4.3	4.5	4.6	4.6	4.5	4.1	39 %
23	G2-W40	4.8	4.7	4.2	4.4	4.6	4.6	4.3	3.9	42 %
24	G2-W55	4.7	4.1	3.8	3.9	4.1	4.1	3.6	3.5	49 %
25	G2-W109	4.1	3.2	3.1	3.2	3.3	3.2	3.1	2.9	57 %

presence of the chamber introduced some impulse reduction. For the remaining models, the I_M at $R = 150$ m were lower compared to those at the chamber entrance, $R = 10$ m, where the I_M initially dropped with R inside the chamber, then rise upon entering the main tunnel. Consider G1-400. The I_M decreased at $R = 30$ m, immediately after the shock waves entered the chamber, then increased and stabilized post $R = 110$ m, noting that the chamber length of G1-400 was 97.2 m. For the second subset, with larger chamber volumes, the I_M at $R = 150$ m were consistently lower than those at $R = 10$ m, as shown in Fig. 14(b). The I_M reduction effects were more pronounced for these models compared to the first subset models.

Similar observations were made for Group (2), as shown in Fig. 15. It is observed that the I_M for all models having chambers by and large decrease with R right after the shock waves move into the chamber, and they increase thereafter and stabilize as the waves propagate into the main tunnel, as described previously.

The relationships between I_M at $R = 150$ m and L_c/W_c for the first two subsets ($H_c = 8.0$ m and 14.9 m) are presented in Fig. 16(a). It becomes evident that across all cases, the I_M decreased as L_c/W_c increased, with no marked overpressure reduction for $L_c/W_c \geq 1.5$. The average I_M for $W = 1000$ kg fell from 3.8 to 1.8 kPa-s for $H_c = 8.0$ m, and to 1.3 kPa-s for $H_c = 14.9$ m. Meanwhile, for $W = 2000$ kg, the average I_M declines were

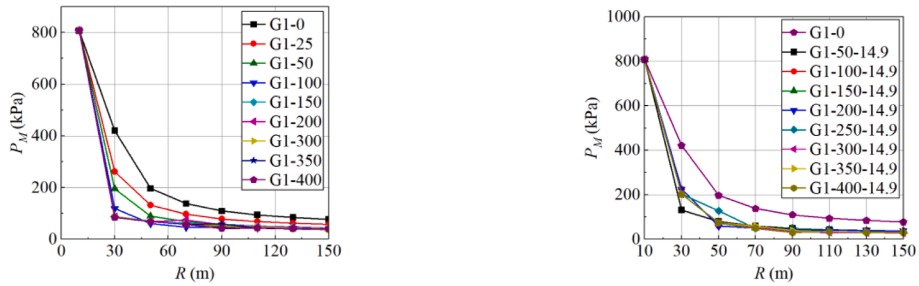

(a) H_c = 8.0 m (b) H_c = 14.9 m

Fig. 10. P_M as a function of R for W = 1000 kg.

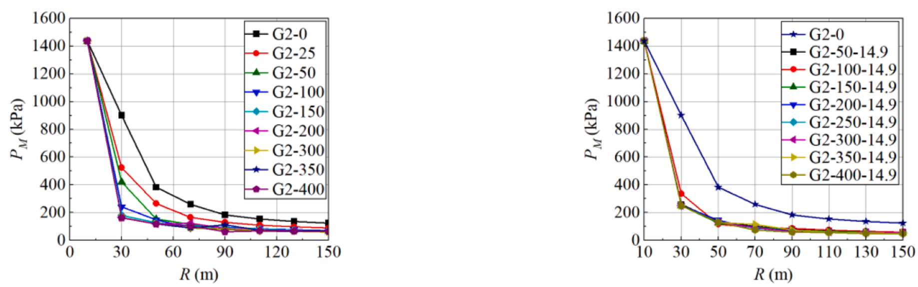

(a) H_c = 8.0 m (b) H_c = 14.9 m

Fig. 11. P_M as a function of R for W = 2000 kg.

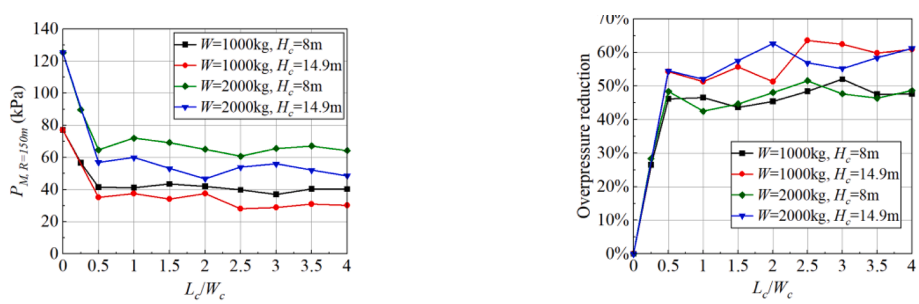

(a) P_M vs L_c/W_c (b) P_M reduction vs L_c/W_c

Fig. 12. P_M and the reduction as a function of L_c/W_c L_c/W_c.

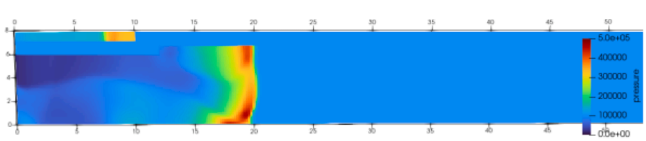

(a) t = 33 ms, G1-400

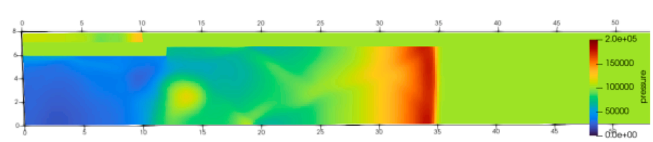

(b) t = 66 ms, G1-400

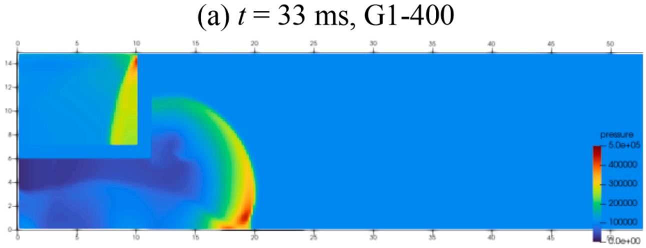

(c) t = 33 ms, G1-400-14.9

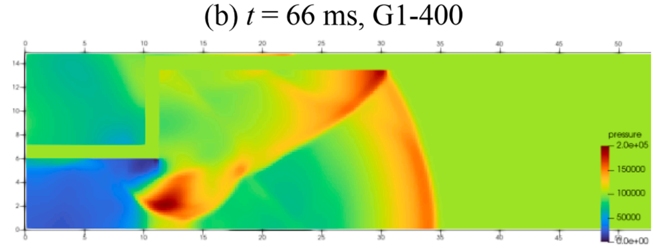

(d) t = 66 ms, G1-400-14.9

Fig. 13. Shock wave propagations for H_c = 8.0 and 14.9 m.

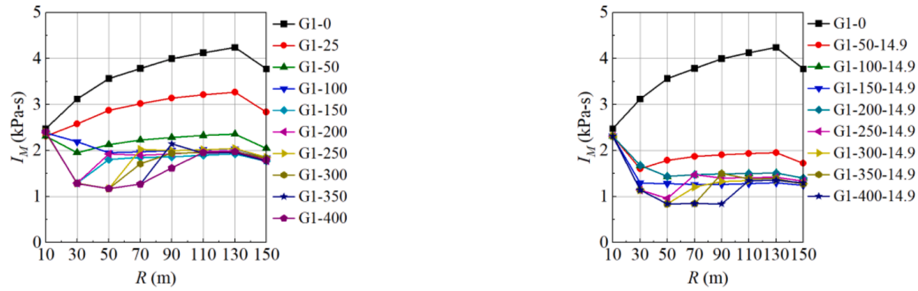

(a) $H_c = 8.0$ m (b) $H_c = 14.9$ m

Fig. 14. I_M as a function of R for $W = 1000$ kg.

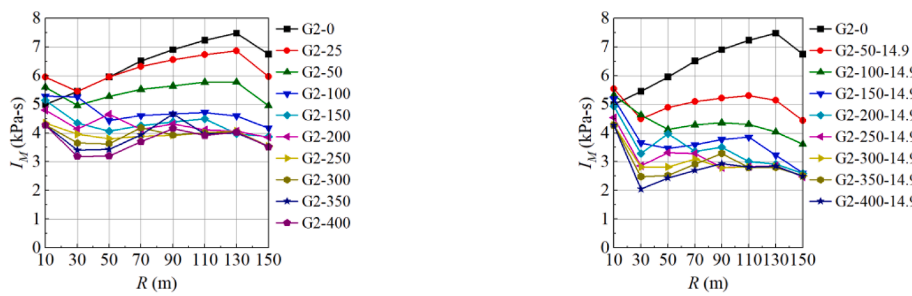

(a) $H_c = 8.0$ m (b) $H_c = 14.9$ m

Fig. 15. I_M as a function of R for $W = 2000$ kg.

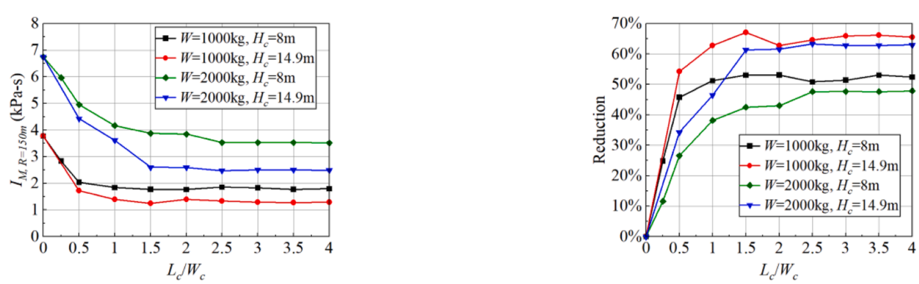

(a) I_M vs L_c/W_c (b) I_M reduction vs L_c/W_c

Fig. 16. I_M as a function of L_c/W_c.

from 6.7 to 3.5 and 2.5 kPa-s, respectively.

Fig. 16(b) shows the results of the I_M reduction at $R = 150$ m as a function of L_c/W_c. The reductions appear nearly consistent independent of charge weight for both chamber heights. For $H_c = 8.0$ m and 14.9 m, the average I_M reductions were around 46 % and 61 %, respectively, indicating a 33 % efficiency increase when the chamber height was increased from 8.0 to 14.9 m.

These results reveal a crucial interplay between chamber geometry

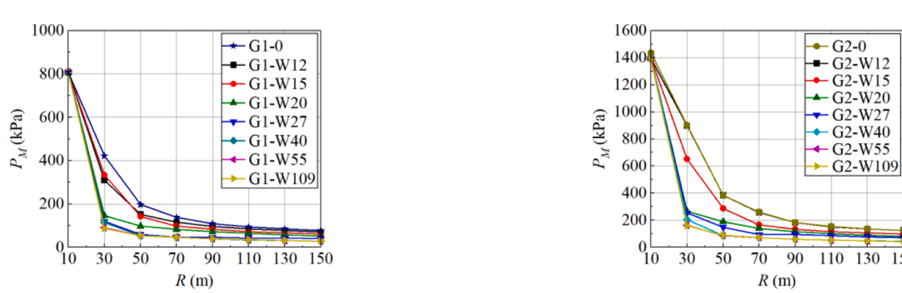

(a) W = 1000 kg (Group 1) (b) W = 2000 kg (Group 2)

Fig. 17. P_M as a function of R varying W_c/W_t.

and impulse mitigation in explosive scenarios. Key findings show that impulses tend to decrease with increasing chamber length-to-width ratio (L_c/W_c) and are significantly impacted by chamber height. For instance, increasing the chamber height from 8.0 m to 14.9 m leads to a notable 33 % increase in impulse reduction efficiency. This trend is consistent across different explosive weights. These observations suggest that optimizing the dimensions of chambers, particularly focusing on height and L_c/W_c ratio, can be a highly effective strategy for reducing the impact of shock waves following a detonation, providing essential insights for the design of safer explosion mitigation systems.

5.3. Maximum overpressure, P_M, as a function of W_c/W_t

Fig. 17 shows the results of the maximum overpressures (P_M) with distance (R) as the ratio of chamber-to-tunnel width (W_c/W_t) changes. With the chamber length and height fixed at 24.3 and 8.0 m, respectively, its width ranged from 10.7 to 97.2 m, corresponding to W_c/W_t of 1.2 to 10.9. It is observed that the P_M with R were attenuated as W_c/W_t increased, stabilizing for $W_c/W_t \geq 2.0$ for both charge weights. Fig. 18 (a) shows the P_M at $R = 150$ m as a function of W_c/W_t. It is seen that the P_M values are minimized for $W_c/W_t \geq 4.5$, where they decreased from 125 to 42 kPa for $W = 1000$ kg and from 79 to 30 kPa for $W = 2000$ kg. Interestingly, as shown in Fig. 18(b), the extent of P_M reductions was consistent irrespective of W: 62 % for $W = 1000$ kg and 63 % for $W = 2000$ kg.

These results highlight that increasing the chamber-to-tunnel width ratio (W_c/W_t) effectively reduces overpressure from detonations. A notable stabilization in overpressure is observed when this ratio exceeds 2.0, emphasizing the importance of chamber width in detonation containment design. This suggests that optimizing the W_c/W_t ratio is crucial for effective blast mitigation.

5.4. Maximum impulse, I_M, as a function of W_c/W_t

Fig. 19 shows the maximum impulses (I_M) with distance (R) based on different width ratio (W_c/W_t). For $W = 1000$ kg, the I_M for G1-0, G1-W12 and G1-W15, namely $W_c/W_t \leq 1.5$, tended to rise with increasing R whereas those for G1-W20 to G1-W109, namely $W_c/W_t \geq 2.0$, showed a decline, as shown in Fig. 19(a). The rise in the I_M values for smaller width ratios was attributed to the effects of shock wave reflections from the side walls, especially as these walls were nearer to the main tunnel edges. A similar pattern was observed for $W = 2000$ kg, as shown in Fig. 19(b).

The relationship between I_M at $R = 150$ m and W_c/W_t are presented in Fig. 20(a). It is seen that the I_M sharply decrease for smaller width ratios, and this decrease becomes gradual for $W_c/W_t \geq 4$ for both charge weights. Specifically, the I_M dropped from 3.8 to 1.0 kPa-s for $W = 1000$ kg, and from 6.7 to 2.9 kPa-s for $W = 2000$ kg. The decline in the I_M was more pronounced for smaller charge weights, showing the maximum reductions of 73 % for W of 1000 kg and 57 % for 2000 kg, as shown in Fig. 20(b).

These results indicate that the chamber-to-tunnel width ratio (W_c/W_t) significantly affects impulse (I_M) in blast scenarios. Smaller W_c/W_t ratios lead to an increase in I_M, likely due to enhanced shock wave reflections from the side walls. In contrast, larger W_c/W_t ratios result in a decrease in I_M, suggesting that wider chambers are more effective in mitigating shock wave impacts. This trend is consistent across different charge weights, highlighting the importance of chamber width in designing effective blast mitigation systems.

5.5. Recommendations for design of expansion chamber

Based on the numerical study, design recommendations for expansion chambers in protective tunnels to mitigate overpressure and impulse are provided. The design considerations primarily focused on three aspects: overpressure stabilization based the concept of overpressure stability introduced in Section 5.1, length-to-width ratio (L_c/W_c L_c/W_c), and width ratio (W_c/W_t). Table 7 provides the proposed ranges for L_c/W_c to achieve the stabilization of overpressures and impulses. For $H_c = 8.0$ m and both charge weights, it was found that both P_M and I_M were effectively stabilized with $L_c/W_c \geq 1.0$. For $H_c = 14.9$ m, the overpressure stabilization was identified within the range of $L_c/W_c \geq 0.5$ for both charge weights, while impulse stabilization required $L_c/W_c \geq 1.0$. In summary, for the protective tunnel in question, it is suggested to keep L_c/W_c values at 1.0 or greater to ensure stabilization of both overpressures and impulses in the expansion chamber.

Table 8 gives the suggested L_c/W_c range for the optimal reduction of P_M and I_M. For W of 1000 kg and H_c of 8.0 m, the P_M reductions for L_c/W_c greater than 0.5 ranged from 44 % to 52 %, averaging 48 %. An increase in H_c to 14.9 m yielded reductions of 51 % to 64 %, averaging 57.5 %, attributed to the additional diffraction effect at the upper corner of the chamber entrance. For W of 2000 kg and L_c/W_c greater than 0.5, the P_M reductions remained consistent, averaging 48 % for H_c of 8.0 m and 58 % for H_c of 14.9 m. It is worth noting the charge weight did not significantly influence overpressure reduction.

Regarding the I_M reductions with W of 1000 kg, the average reductions at L_c/W_c greater than 0.5 were roughly 50 % and 61 % for H_c of 8.0 m and 14.9 m, respectively. In contrast, for W of 2000 kg, achieving average reductions of approximately 43 % and 62 % required L_c/W_c L_c/W_c exceeding 1.0 and 1.5 for H_c of 8.0 and 14.9 m, respectively. Considering the assessed blast scenarios and protective tunnels, it is recommended to consider L_c/W_c ratios greater than 1.5 for effective mitigation of both P_M and I_M.

For the effect of the width ratio, the effective reductions for P_M were observed when W_c/W_t exceeded 4.0 for both charge weights, as presented in Table 9, noting that these reductions averaged approximately 63 % for both charge weights. On the other hand, the I_M reductions varied with the charge weight. For W_c/W_t exceeding 4.5, the average reductions were 68 % for W of 1000 kg and 50 % for W of 2000 kg.

Since the variables L_c/W_c, W_c/W_t and H_c are directly related to the

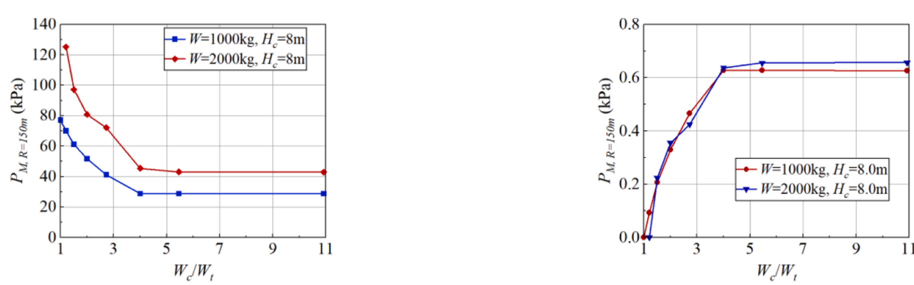

(a) P_M vs W_c/W_t

(b) P_M reduction vs W_c/W_t

Fig. 18. P_M as a function of R for $W = 1000$ kg.

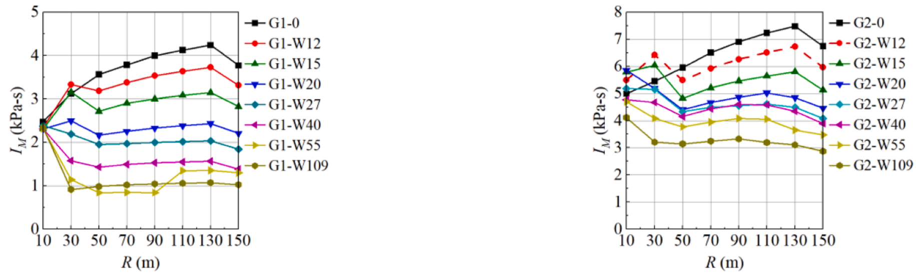

(a) $W = 1000$ kg (a) $W = 2000$ kg

Fig. 19. I_M as a function of R.

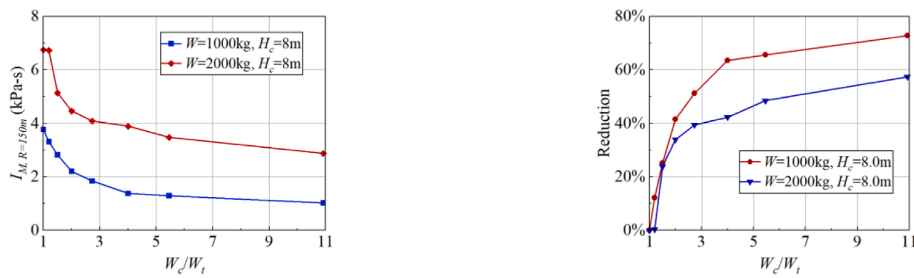

(a) I_M vs W_c/W_t (b) I_M reduction vs W_c/W_t

Fig. 20. I_M as a function of R for W of 2000 kg.

Table 7
Proposed range of L_c/W_c L_c/W_c for P_M and I_M stabilization.

	$W = 1000$ kg (Group (1))		$W = 2000$ kg (Group (2))	
	$H_c = 8.0\ m$	$H_c = 14.9\ m$	$H_c = 8.0\ m$	$H_c = 14.9\ m$
P_M	$L_c/W_c \geq 1.0$	$L_c/W_c \geq 0.5$	$L_c/W_c \geq 1.0$	$L_c/W_c \geq 0.5$
I_M	$L_c/W_c \geq 1.0$	$L_c/W_c \geq 1.0$	$L_c/W_c \geq 1.0$	$L_c/W_c \geq 1.0$

Table 8
Proposed range of L_c/W_c L_c/W_c for P_M and I_M reductions.

	Proposed range				Reduction (%)			
	$W = 1000$ kg (Group (1))		$W = 2000$ kg (Group (2))		$W = 1000$ kg (Group (1))		$W = 2000$ kg (Group (2))	
	$H_c = 8.0\ m$	$H_c = 14.9\ m$	$H_c = 8.0\ m$	$H_c = 14.9\ m$	$H_c = 8.0\ m$	$H_c = 14.9\ m$	$H_c = 8.0\ m$	$H_c = 14.9\ m$
P_M	$L_c/W_c \geq 0.5$	$L_c/W_c \geq 0.5$	$L_c/W_c \geq 0.5$	$L_c/W_c \geq 0.5$	44 % to 52 %	51 % to 64 %	43 % to 52 %	52 % to 63 %
I_M	$L_c/W_c \geq 0.5$	$L_c/W_c \geq 0.5$	$L_c/W_c \geq 1.0$	$L_c/W_c \geq 1.5$	46 % to 53 %	54 % to 67 %	38 % to 48 %	61 % to 63 %

Table 9
Proposed range of W_c/W_t for P_M and I_M reductions.

	Proposed range		Reduction (%)	
	$W = 1000$ kg (Group (1))	$W = 2000$ kg (Group (2))	$W = 1000$ kg (Group (1))	$W = 2000$ kg (Group (2))
P_M, $R = 150\ m$	$W_c/W_t \geq 4$	$W_c/W_t \geq 4$	63 %	64 % to 66 %
I_M, $R = 150\ m$	$W_c/W_t \geq 4.5$	$W_c/W_t \geq 4.5$	63 % to 73 %	42 % to 57 %

chamber's volume and the blast wave energy dissipation by the chamber is fundamentally linked to its volume, the effects of the volume on overpressure and impulse reductions were examined. As shown in Fig. 21, it is evident that both overpressure and impulse reductions significantly increase with the chamber's volume, showing a convergence trend above approximately 10,000 m^3. Further, for chamber volumes greater than 20,000 m^3, this convergence is pronounced, regardless of the explosive weight.

A design example for the expansion chamber is provided. For the given tunnel, which has the width of 8.9 m as shown in Fig. 2, and following the above recommendations, the chamber width was determined to be four times the tunnel width, resulting in 35.6 m. The length was set at 1.5 times the width, giving 53.4 m, and the height was established at 14.9 m. These dimensions result in the chamber volume of 28,326 m^3. According to Fig. 21, this specific chamber volume is projected to offer the greatest reduction in overpressure and impulse for this tunnel design.

In summary, this numerical study offers design recommendations for expansion chambers in protective tunnels, focusing on mitigating overpressure and impulse from detonations. Key insights include the importance of maintaining an optimal length-to-width ratio (L_c/W_c) and width ratio (W_c/W_t) in the chamber design. Higher L_c/W_c values are crucial for stabilizing overpressure and impulse, with specific ratios varying based on chamber height and explosive weight. Additionally, a higher W_c/W_t ratio is identified as significant in effectively reducing both overpressure and impulse. These findings highlight the critical role of chamber geometry in designing protective tunnels, emphasizing the need to balance various dimensional aspects for optimal explosion mitigation.

It also needs to be noted that regarding the focus on a specific distance between the detonation point and the expansion chamber was chosen to analyze the shock wave behavior and chamber efficacy at a scaled distance, as detailed in Section 3. While this distance influences the shock wave's transition to a 1D form, future research could explore varying distances to deepen the understanding of shock wave

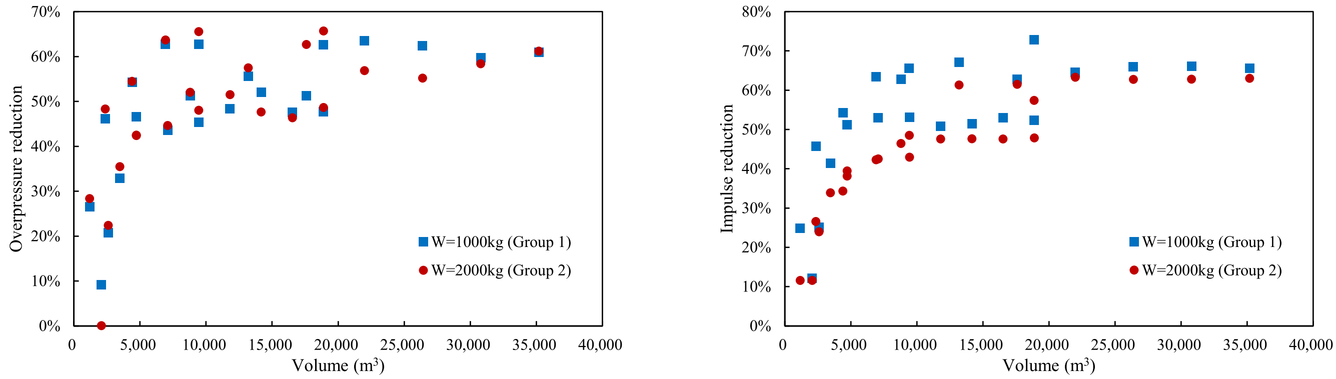

(a) Overpressure reduction (b) Impulse reduction

Fig. 21. Overpressure and impulse reductions as a function of expansion chamber volume.

propagation in relation to chamber placement. Such exploration would significantly contribute to the development of more effective blast mitigation strategies.

6. Conclusion

A study was conducted using the CFD code, Viper::Blast, to investigate the effects of overpressure and impulse mitigation in protective tunnels based on the geometry of an expansion chamber. The findings demonstrate a significant improvement in overpressure and impulse reduction, attributable to the optimized design parameters of the expansion chamber. By conducting numerical simulations using Viper::Blast, the CFD model was validated using the empirical design charts available in UFC 3–340-02. The presented modeling methodology holds significant value for the blast-resistant design of protective tunnels, ensuring the safety of underground facilities.

Based on the CFD analysis, an expansion chamber with the L_c/W_c ratio exceeding 1.0 is recommended for stabilizations of blast overpressures and impulses. Within this range, the maximum overpressures (P_M) and impulses (I_M) in protective tunnels subjected to detonations showed rapid stabilization. For effectively mitigating the P_M and I_M in protective tunnels, the L_c/W_c ratios should exceed 1.5, given the tunnel specifications and blast scenarios of this study.

Chamber cross-sectional dimensions also plays a critical role in blast mitigation. It was observed that overpressure and impulse reductions increased significantly with chamber height and width. The 8.0-m chamber height yielded 43 % to 50 % reductions, while the 14.9-m height achieved 58 % to 62 % reduction, noting that both overpressure and impulse reductions increased by 20 % to 44 % as the chamber height increased. The W_c/W_t ratio also significantly affected the blast overpressure and impulse mitigation due to the diffraction effect of blast waves. With the width ratio of 4.0 or greater, the P_M decreased by 63 % to 65 % for both charge weights. Further, with the width ratios exceeding 4.5, the I_M were reduced by 50 % to 68 %. Considering the greater diffraction and reduced reflection of blast waves within the chamber, it is crucial to acknowledge their impact on P_M and I_M reductions.

This study enhances the understanding of blast wave dynamics and delivers actionable recommendations for designing expansion chambers in tunnels. It surpasses existing studies by thoroughly evaluating chamber design parameters, contributing significantly to the development of more efficient and cost-effective blast mitigation strategies. The results underscore the effectiveness of expansion chambers in improving safety in underground settings against high explosive detonations, laying a solid groundwork for future advancements in blast-resistant infrastructure for subterranean facilities.

CRediT authorship contribution statement

Jinwon Shin: Conceptualization, Data curation, Formal analysis, Funding acquisition, Investigation, Methodology, Software, Validation, Writing – original draft. **Seungki Pang:** Data curation, Formal analysis, Investigation, Methodology, Software, Validation, Visualization, Writing – original draft. **Woosuk Kim:** Conceptualization, Formal analysis, Resources, Supervision, Visualization, Writing – review & editing.

Declaration of competing interest

The authors declare that they have no known competing financial interests or personal relationships that could have appeared to influence the work reported in this paper.

Data availability

Data will be made available on request.

Acknowledgements

This research was supported by the National Research Foundation of Korea (NRF) grant funded by the Korea government (MSIT) (No. 2021R1C1C1012833).

References

Angelides, S., Burgan, B., Kyprianou, C., Rigby, S., Tyas, A., 2022. EMBlast: a software for rapidly and accurately predicting blast loads on structures. 97th Conference of the International Committee for Industrial Construction (CICIND).
Angelides, S.C., Morison, C., Burgan, B.A., Kyprianou, C., Rigby, S.E., Tyas, A., 2023. A methodology for predicting far-field blast loading on structures. Structures.
ANSYS, 2018. ANSYS Autodyn User's Manual 19.0. ANSYS, Inc, Canonsburg, PA.
ANSYS, 2005. Remapping Tutorial, Revision 4.3. ANSYS, Inc. Canonsburg, PA.
ASME, 2006. Guide for verification and validation in computational solid mechanics. American Society of Mechanical Engineers.
Bai, F., Liu, Y., Yan, J.-B., Xu, Y.-L., Shi, Z.-Q., Huang, F.-L., 2022. Study on the characteristics of blast loads due to two simultaneous detonated charges in real air. Int. J. Non Linear Mech. 146, 104108.
Baker, W., Cox, P., Westine, P., Kulesz, J., Strehlow, R., 1983. Fundamental studies in engineering. In: Explosion Hazards and Evaluation. Elsevier Amsterdam, Oxford, New York, pp. 238–243.
Benselama, A.M., Mame, J.-P., Monnoyer, F., Proust, C., 2010. A numerical study of the evolution of the blast wave shape in tunnels. J. Hazard. Mater. 181, 609–616.
Brode, H.L., 1959. Blast wave from a spherical charge. The Physics of Fluids. 2, 217–229.
Castellano, A.J., Caltagirone, J.P., Sock, F.E., Dobbs, N., RESEARCH, A.A., MO, D.C.S.L., 1982. Structures to Resist the Effects of Accidental Explosions (TM 5-1300, NAVFAC P-397, AFM 88-22). Revision of Tri-Service Regulatory Design Manual. Washington, DC.
Cook, R.D., 2002. Concepts and applications of finite element analysis, vol. John wiley & sons.

Curran, D.R., 1996. Underground storage of ammunition: experiments concerning accidental detonation in an underground chamber. Norwegian Defense Research Establishment.

Dennis, A.A., Rigby, S.E., 2023. The direction-encoded neural network: a machine learning approach to rapidly predict blast loading in obstructed environments. International Journal of Protective Structures. (20414196231177364).

Dennis, A., Stirling, C., Rigby, S., 2023. Towards the development of machine Learning tools for blast load prediction. Proceedings of the 6th International Conference on Protective Structures (ICPS6).

Denny, J., Langdon, G., Rigby, S., Dickinson, A., Batchelor, J., 2022. A numerical investigation of blast-structure interaction effects on primary blast injury risk and the suitability of existing injury prediction methods. International Journal of Protective Structures. (20414196221136157).

Dobratz, B., Crawford, P., 1981. LLNL explosives handbook: properties of chemical explosives and explosive simulants: UCRL-52997. Livermore,(CA).

DoD, 2008. Unified Facilities Criteria (UFC): Structures to Resist the Effects of Accidental Explosions (UFC 3-340-02). Departments of Defense, Washington, DC.

Dusenberry, D.O., 2010. Handbook for Blast-Resistant Design of Buildings.

Fedorov, A., Kratova, Y.V., Khmel', T., 2008. Numerical study of shock-wave diffraction in variable-section channels in gas suspensions. Combustion, Explosion, and Shock Waves. 44, 76–85.

Fickett, W., Davis, W.C., 2000. Detonation: theory and experiment.

Gabriel, S., Denny, J., Chung Kim Yuen, S., Langdon, G.S., Govender, R.A., 2023. The effect of scaling building configuration blast experiments on positive phase blast wave parameters. Appl. Sci. 13, 5956.

Hager, K., Birnbaum, N., CA, N.F.E.S.C.P.H. 1996. Calculation of the internal blast pressures for tunnel magazine tests. Proceedings of the 27th DoD Explosives Safety Seminar.

Han, K.-C., Jang, H.-D., Kim, W.-B., Yang, H.-S., Jang, M.-H., 2010. A study on the damage to a mine drift caused by blast welding. ISRM International Symposium-Asian Rock Mechanics Symposium.

Henrych, J., Major, R., 1979. The dynamics of explosion and its use elsevier. Scientific Publishing Company, Amsterdam.

Hetherington, J., Smith, P., 1994. Blast and ballistic loading of structures, Vol., Crc Press.

Heylmun, J., Vonk, P., Brewer, T., 2019. blastFoam Theory and User Guide Version 2.0.0. Synthetik Applied Technologies, Austin, TX.

Isaac, O.S., Alshammari, O.G., Pickering, E.G., Clarke, S.D., Rigby, S.E., 2022. Blast wave interaction with structures–an overview. International Journal of Protective Structures. (20414196221118595).

Kalubadanage, D., Remennikov, A., Ngo, T., Qi, C., 2020. Close-in blast resistance of large-scale auxetic re-entrant honeycomb sandwich panels. J. Sandw. Struct. Mater. 23, 4016–4053.

Kingery, C.N., Bulmash, G., 1984. Airblast parameters from TNT spherical air burst and hemispherical surface burst, vol. US Army Armament and Development Center. Ballistic Research Laboratory.

Kingery, C., Pannill, B., 1964. Peak overpressure vs scaled distance for TNT surface bursts (hemispherical charges). BRL Memorandum Report. 1518, 1–22.

Kingery, C.N., 1966. Air blast parameters versus distance for hemispherical TNT surface bursts, Vol., Ballistic Research Laboratories Aberdeen Proving Ground, MD.

Kinney, G.F., Graham, K.J., 1962. Explosive shocks in air, vol. Springer Science & Business Media, New York.

Kinney, G.F., Graham, K.J., Raspet, R., 1986. Explosive shocks in air, by Gilbert F. Acoustical Society of America, New York, Kinney and Kenneth J. Graham.

Králik, E.J., Baran, M., 2013. Numerical analysis of the exterior explosion effects on the buildings with barriers. Appl. Mech. Mater. 390, 230–234.

Krauthammer, T., 2008. Modern protective structures, Vol. 22, Crc Press.

Liu, J., Yan, Q., Wu, J., 2008. Analysis of blast wave propagation inside tunnel. Transactions of Tianjin University. 14, 358–362.

LST, 2021. LS-DYNA Manual R13.0 Livermore Software Technology (LST), An ANSYS Company, Michigan.

Machniewski, P., Molga, E., 2022. CFD analysis of large-scale hydrogen detonation and blast wave overpressure in partially confined spaces. Process Saf. Environ. Prot. 158, 537–546.

Mandal, J., Goel, M., Agarwal, A., 2019. Numerical simulation of underwater subway tunnel subjected to internal blast loading. In: Advances in Engineering Materials, Structures and Systems: Innovations, Mechanics and Applications. CRC Press, pp. 767–772.

Marks, N.A., Stewart, M.G., Netherton, M.D., Stirling, C.G., 2021. Airblast variability and fatality risks from a VBIED in a complex urban environment. Reliab. Eng. Syst. Saf. 209, 107459.

Mills, C. 1987. The design of concrete structures to resist explosions and weapon effects. 1st International Conference on Concrete for Hazard Protections, Edinburgh, UK.

Mohotti, D., Wijesooriya, K., Weckert, S., 2023. A simplified approach to modelling blasts in computational fluid dynamics (CFD). Defence Technology. 23, 19–34.

Mussa, M.H., Mutalib, A.A., Hamid, R., Raman, S.N. 2020. Advanced dynamic response analysis of under-ground tunnel affected by blast ground distance. The 5th International Technical Conference (ITC).(Malaysia. 2020).

National Information Resources Service, 2016. https://www.nirs.go.kr/eng/index.jsp.

Pang, S.-K., Shin, J.-W., Kim, W.-D., 2018. Evaluation of pressure effects on blast valves for facility protection of underground computing center. Journal of the Korean Society for Geothermal and Hydrothermal Energy. 14, 21–28.

Pang, S., Shin, J., 2021. Blast overpressure evaluation for blast valves in protective tunnels with rectangular-shaped tunnel entrances. Journal of the Korean Society for Geothermal and Hydrothermal Energy. 17, 79–90.

Pennetier, O., William-Louis, M., Langlet, A., 2015. Numerical and reduced-scale experimental investigation of blast wave shape in underground transportation infrastructure. Process Saf. Environ. Prot. 94, 96–104.

Rose, T.A., 2010. An approach to the evaluation of blast loads on finite and semi-infinite structures Cranfield University].

Sharma, P., Patel, B., Lal, H., 2016. Blast valve design and related studies: a review. Def. Sci. J. 66.

Sherkar, P., 2010. Modeling the effects of detonations of high explosives to inform blast-resistant design, vol. State University of New York at Buffalo.

Shin, J., 2014. Air-blast effects on civil structures, vol. State University of New York at Buffalo.

Shin, J., Whittaker, A., Cormie, D., Aref, A. 2015a. Verification and validation of a CFD code for modeling detonations of high explosives. Proceedings of the 16th International Symposium for the Interaction of the Effects of Munitions with Structures. University of Florida, Gainesville, FL, USA.

Shin, J., Lee, K., 2016. A Numerical analysis for blast pressure and impulse from free-air burst. Journal of Korean Society of Steel Construction. 28, 271–280.

Shin, J., Pang, S., 2022. Blast overpressure reduction using entrance shape and blast pocket depth of protective tunnels. Journal of Korean Society of Steel Construction. 34, 25–33.

Shin, J., Whittaker, A.S., Cormie, D., Wilkinson, W., 2014. Numerical modeling of close-in detonations of high explosives. Eng. Struct. 81, 88–97.

Shin, J., Whittaker, A.S., Cormie, D., 2015b. Incident and normally reflected overpressure and impulse for detonations of spherical high explosives in free air. J. Struct. Eng. 141, 04015057.

Shin, J., Pang, S., Kim, D.-K., 2023. Effects of entrance shape and blast pocket on internal overpressure mitigation for protective tunnels exposed to external detonation on the ground. Appl. Sci. 13, 1759.

Silvestrini, M., Genova, B., Trujillo, F.L., 2009. Energy concentration factor. a simple concept for the prediction of blast propagation in partially confined geometries. J. Loss Prev. Process Ind. 22, 449–454.

Skews, B., Law, C., Muritala, A., Bode, S., 2012. Shear layer behavior resulting from shock wave diffraction. Exp. Fluids 52, 417–424.

Smith, P., Hetherington, J., 1994. Blast and ballistic loading of structures. Butterwirth. Heinemann, Elsevier Science Ltd. https://www.gurit.com.

Smith, A.C., Sapko, M.J., 2005. Detonation wave propagation in underground mine entries. Journal of the Mine Ventilation Society of South Africa. 58, 20–25.

Stirling, C.G., 2020. Viper: blast Summary. Stirling Simulation Services Limited, United Kingdom, pp. 1–34.

Stirling, C.G., 2021. Viper: blast user manual and examples for version 1.20.0, Commercial in confidence. Stirling Simulation Services Limited, Glasgow, United Kingdom.

Vaghefi, M., Mobaraki, B., 2021. Evaluation of the effect of explosion on the concrete bridge deck using LS-DYNA. Int. Rev. Civ. Eng. 12, 135.

Wada, Y., Liou, M.-S., 1994. A flux splitting scheme with high-resolution and robustness for discontinuities. 32nd Aerospace Sciences Meeting and Exhibit.

Zhao, X., Chen, C., Shi, C., Chen, J., Chen, Q., Zhao, D., 2021. A three-dimensional simulation of the effects of obstacle blockage ratio on the explosion wave in a tunnel. J. Therm. Anal. Calorim. 143, 3245–3256.

Zhao, B.-L., Cui, C.-Y., Chen, J.-P., Wang, Y., 2015. Numerical simulation about the effect of tunnel expansion chamber on the shock wave attenuation. 4th International Conference on Computer, Mechatronics, Control and Electronic Engineering.